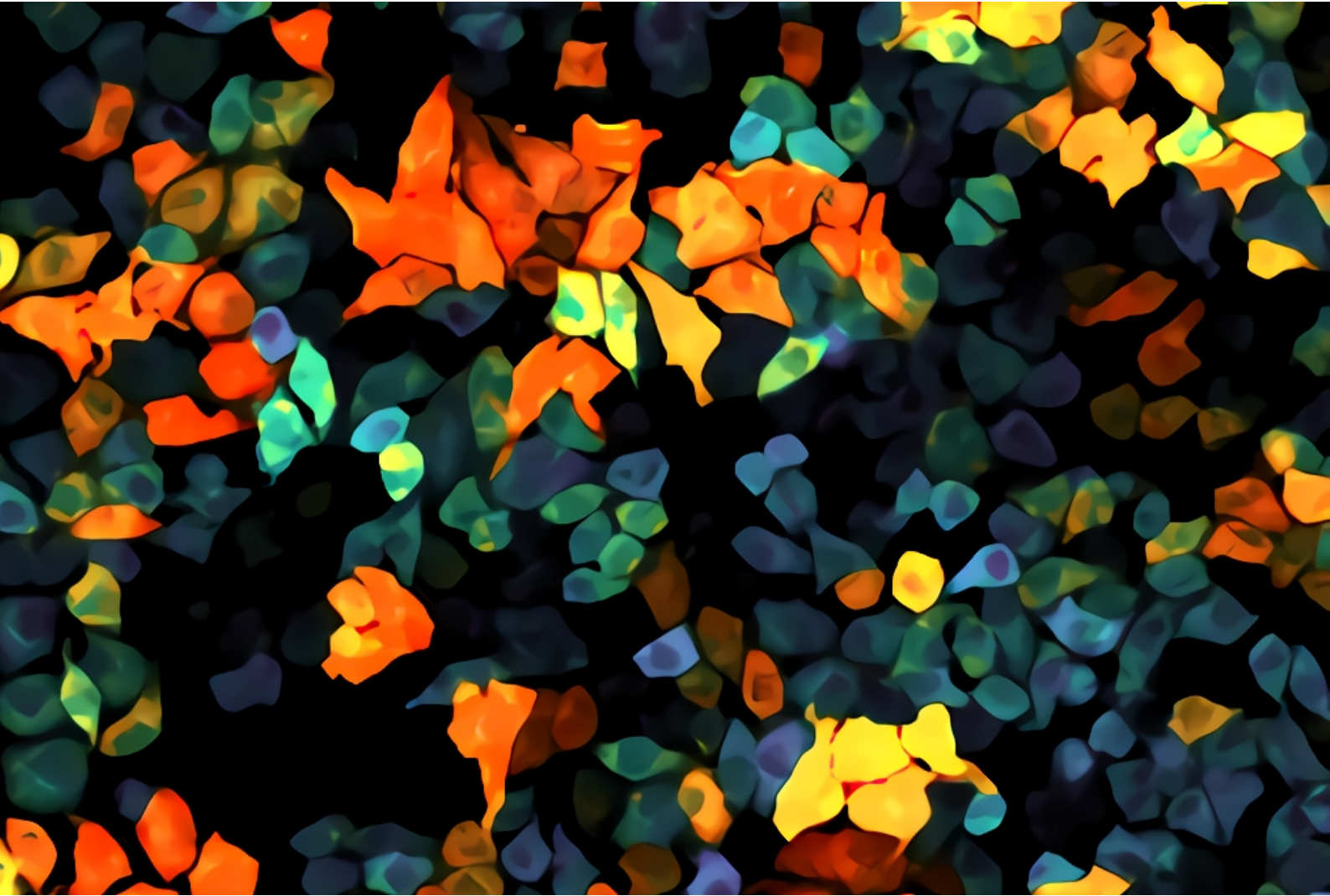# Studying the effects of microenvironmental variables on the cAMP signaling pathway using FRET-FLIM

W.H.J. Elling

Ward Elling
5871581
w.h.j.elling@students.uu.nl

Studying the effects of microenvironmental variables on the cAMP signaling pathway using FRET-FLIM

W.H.J. Elling[1,2,3]

Abstract

Cell behavior is regulated by variables within its local microenvironment, which includes soluble biochemical molecules like receptor ligands or molecular oxygen (O_2), as well as physical properties like temperature. Cells respond to such microenvironmental variables through intracellular biochemical signaling cascades, ultimately altering cellular behavior. A major example of such a pathway is the well-studied 3',5'-cyclic adenosine monophosphate (cAMP) pathway, in which cAMP is produced in response to numerous soluble biochemical molecules. However, how this cAMP signaling pathway is affected by varying oxygen concentration or temperature has not been well-described. Therefore, this study aims to (1) investigate the effects of hypoxia on cAMP pathway activation and breakdown, and (2) investigate the effects of elevated temperature on cAMP signaling dynamics. In both projects, Fluorescence Lifetime Imaging Microscopy (FLIM) was used to quantify rapid changes in Fluorescence Resonance Energy Transfer (FRET) efficiency in cells stably expressing the EPAC-based cAMP FRET-FLIM biosensor, EPAC-S^{H201}, in real-time. In the hypoxia-section of this report, the use of a custom-build hypoxia chamber that allows for real-time imaging and manipulation of cells in hypoxic conditions is highlighted first. Next, it is shown that no hypoxia-induced effects on receptor-mediated cAMP pathway activation were observed. Furthermore, no hypoxia-induced effects on cAMP breakdown time were found. Despite this, it is ultimately concluded that real-time FRET-FLIM is an asset to the current field of hypoxia research. In the temperature-section of this report, it is first shown that cAMP biosensor FRET efficiency changes in cells subjected to elevated temperatures. Numerous different approaches were performed to control whether the change in FRET efficiency is caused by the production of cAMP. However, it is ultimately concluded that the change in FRET efficiency is instead caused by a heat-induced biosensor artifact, meaning this specific biosensor cannot be used to study cAMP signaling dynamics in response to temperature deviations.

Keywords

3',5'-cyclic adenosine monophosphate (cAMP); G protein coupled receptor (GPCR); Phosphodiesterase (PDE); Fluorescence Resonance Energy Transfer (FRET); Fluorescence Lifetime Imaging Microscopy (FLIM); cAMP FRET-FLIM biosensor; Molecular oxygen (O_2); Hypoxia; Temperature

[1] Department of Cell Biology, The Netherlands Cancer Institute, Amsterdam, The Netherlands
[2] Molecular and Cellular Life Sciences, Graduate School of Life Sciences, Utrecht University, Utrecht, The Netherlands
[3] Author of this general research profile internship report in the laboratory of Dr. K. Jalink. Student number: 5871581. E-mail: w.h.j.elling@students.uu.nl. Host institute supervisor: Dr. K. Jalink. Daily supervisor: Dr. O. Kukk. Examiner: Dr. T. Dansen.

Introduction

The cyclic AMP signaling pathway

The behavior of individual cells within a multicellular organism is tightly regulated by stimuli from their local environment. Cells can sense a variety of environmental stimuli, including intricate biochemical signals such as receptor agonists and respond to them through intracellular signaling cascades that ultimately alter gene expression. Thereby, these intracellular signaling cascades regulate important physiological processes, such as cell proliferation, cell differentiation and maintenance of homeostasis, and dysregulation of these signaling cascades can contribute to various diseases, including cancer. An example of such an intracellular signaling transduction pathway is the 3',5'-cyclic adenosine monophosphate (cAMP) pathway, in which cAMP is generated upon activation of a G protein coupled receptor (GPCR) and acts as a second messenger, influencing various important cellular processes like proliferation and differentiation[1–4]. The human genome encodes for hundreds of different GPCRs that each respond to different instructive cues, including hormones, growth factors and neurotransmitters, and are commonly targeted by drugs, emphasizing the importance of the cAMP signaling pathway[5].

GPCRs are coupled to a heterotrimeric αβγ G-protein complex (Figure 1A). Upon interaction between a ligand and its targeted GPCR, the GPCR undergoes a conformational change which results in the exchange of GDP for GTP on the αβγ G-protein complex, causing the subsequent dissociation of the G_α protein from the βγ subunits[1–3]. The activated G_α protein can either stimulate or inhibit the production of cAMP from ATP by adenylyl cyclase (AC), depending on whether the activated GPCR was coupled to G_α proteins of the stimulatory $G_{\alpha s}$ family or the inhibitory $G_{\alpha i}$ family[1,2]. In case ACs are stimulated by $G_{\alpha s}$ proteins, the produced cAMP can bind to and activate several effector proteins, which include the important and well-studied protein kinase A (PKA) as well as guanine nucleotide exchange factors from the EPAC family[1–4,6]. PKA is a tetramer which consists of two regulatory subunits and two catalytic subunits. The catalytic subunits dissociate from the complex upon binding of cAMP to the regulatory subunits, which allows the now active catalytic subunits to phosphorylate other proteins[1–4]. Importantly, the active catalytic subunits can translocate to the nucleus where they activate the transcription factor cAMP response element-binding protein (CREB), which binds to cAMP response elements in promotor and enhancer regions of target genes to alter their gene transcription[1–3]. To maintain a tight regulation of intracellular cAMP levels, cells make use of phosphodiesterase (PDE) enzymes, which break the cyclic phosphodiester bond in cAMP to convert it into AMP[1–4].

A FRET-FLIM cAMP biosensor

Because of the importance of the cAMP signaling pathway in regulating cellular behavior, extensive research efforts have been made to unravel its intricate signaling dynamics. To this end, several research groups have developed fluorescent biosensors that allow for visualization and quantification of cAMP signaling dynamics in living cells with high spatial and temporal resolution, utilizing Fluorescence Resonance Energy Transfer (FRET) as a readout[7–11]. FRET is a mechanism in which energy is transferred between adjacent donor and acceptor fluorophores through nonradiative dipole-dipole coupling, which is dependent on the distance between the adjacent fluorophores (<10 nm), their respective dipole orientation, and spectral overlap between donor emission and acceptor absorption[12–15]. FRET-based cAMP biosensors commonly contain a cAMP-binding domain that is flanked by a donor fluorophore and an acceptor fluorophore[7–11]. The biosensor will undergo a conformational change upon interaction between cAMP and the cAMP-binding domain, which increases the distance between the two fluorophores and therefore decreases FRET between them (Figure 1B). Thus, a change in FRET can be used as a readout for cAMP levels.

FRET is commonly detected by changes in the ratio between donor and acceptor fluorescence intensity[4,10,11,13]. The main advantage of this method is that it can be performed on widely-available widefield or confocal fluorescence microscopes and spectroscopes. However, ratiometric measurements are not truly quantitative due to imaging artifacts like donor bleedthrough and directly excited acceptors, unless extensive controls and corrections are performed[4,10,11,13,14,16,17]. In many cases an alternative method of measuring FRET, Fluorescence Lifetime Imaging Microscopy (FLIM), offers advantages over FRET detection by ratiometry. This method focusses on detecting the
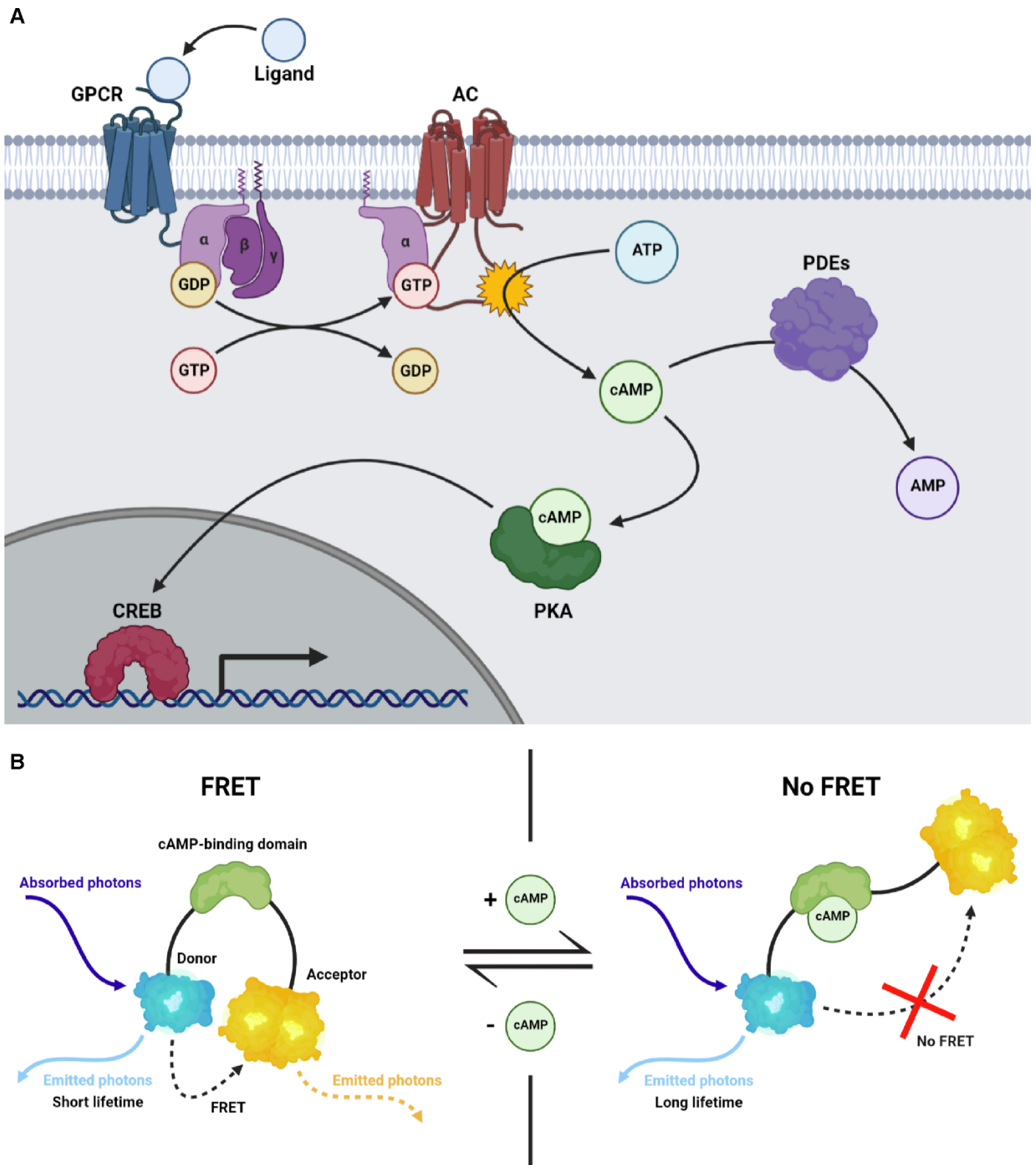
Figure 1. The cAMP signaling pathway and a FRET biosensor for cAMP.
(A) A schematic illustration of the cAMP signaling pathway. The cAMP pathway is activated upon binding of a ligand to its specific GPCR. The activated GPCR mediates the exchange of GDP for GTP bound to the αβγ G-protein complex, causing the dissociation of the Gα protein from the βγ subunits. The dissociated Gα protein stimulates adenylyl cyclase to synthesize cAMP from ATP. cAMP activates several downstream effector proteins, including PKA, which ultimately regulates the activity of downstream enzymes and transcription factors, including the transcription factor CREB. cAMP is hydrolyzed into AMP by phosphodiesterase enzymes. (B) A schematic illustration of the EPAC-based FRET-FLIM biosensor for cAMP. In absence of cAMP, the biosensor is in a conformation where FRET occurs between the donor and acceptor fluorophores, causing the donor excited state lifetime to be short. When cAMP is bound to the biosensor, it undergoes a conformational change in which the donor and acceptor fluorophores will no longer be able to FRET, causing the donor excited state lifetime to increase.

average time the donor fluorophore remains in its excited state. During FRET, the interaction between the donor and acceptor fluorophore shortens the excited-state lifetime of the donor fluorophore (Figure 1B)[4,10–13,15,17,18]. A useful analogy to understand this principle is the following: imagine repeatedly throwing a bouncing ball into a bucket with a hole in its bottom, and measuring the average time it takes for the ball to fall through the hole. Adding a second hole to the bottom of the bucket increases the chance the ball bounces through a hole, and thus decreases the average time it takes for the ball to fall out of the bucket. During FRET, the acceptor fluorophore functions as the second hole in this analogy, offering the excited donor fluorophore a second mechanism to lose its excess energy and return to its ground state. This decreases the average time the donor remains in its excited state. Therefore, donor fluorescence lifetime can be used to quantify FRET in biosensors. FRET-FLIM measurements are more quantitative and robust compared to ratiometric measurements, because donor lifetime is direct measurement for FRET efficiency without the interference of donor bleedthrough or directly excited acceptors[4,10,11,13,15,17,18]. Additionally, focus drift is less detrimental to FRET-FLIM quantification compared to ratiometric FRET quantification[19]. The major drawback of FRET-FLIM is that it requires expensive dedicated equipment to measure single donor photon lifetimes, which are in the order of nanoseconds[4,10,11,13,17]. However, continued developments in FLIM instrumentation and simplification of quantitative FLIM data extraction and analysis are opening up FRET-FLIM to a broader range of users[4,20–23].

Fluorescence lifetimes can be detected through different methods. Two examples of such methods are time-domain FLIM (TD-FLIM) by time correlated single photon counting (TCSPC) and frequency-domain FLIM (FD-FLIM). In TD-FLIM by TCSPC, the sample is scanned using a high-frequency pulsed light source, after which the arrival times of single photons with respect to the pulsed light source are detected. This method offers the highest time resolution, lifetime accuracy and photon efficiency of any lifetime detection method and is often used on confocal laser scanning microscopes[15,17,18]. In FD-FLIM, the sample is illuminated by a modulated light source. The fluorescence lifetime is determined by the phase shift and decreased modulation depth of the fluorescence emission compared to the modulated light source[15,17,18]. Since FD-FLIM does not take single photon events into account, only the total fluorescence signal, FD-FLIM is able to work at high fluorescence intensities where TCSPC becomes less optimal, such as on widefield systems[18].

The latest generation of cAMP biosensors is optimized for FRET-FLIM and displays an exceptional fluorescence lifetime change (>80%)[11]. It consists of a near full-length cAMP-binding EPAC1 protein that contains mutations that render it catalytically dead, a single point mutation (Q270E) that increases affinity for cAMP, and finally a deletion of the membrane-targeting DEP domain[11]. The EPAC1 is flanked by a donor mTurquoise2, a bright and photostable fluorophore, and by a tandem of dark, circular permutated ^{cp173}Venus fluorophores as acceptor[11,24]. Since only the donor lifetime is measured in FRET-FLIM, the use of dark (non-emitting) acceptors offers several advantages, such as allowing measurement of a boarder part of the donors emission spectrum, which increases brightness and allows for decreased phototoxicity[4,11,13,15]. Upon binding of cAMP to the EPAC1 domain, a conformational change in the biosensor will pull the two fluorophores apart, decreasing FRET and therefore increasing the average donor lifetime (Figure 1B)[4,11]. This latest generation EPAC-based cAMP biosensor (mTurq2-EPAC(CD,ΔDEP,Q270E)-tdblcpVenus) will be used to study cAMP signaling dynamics in this report and will be referred to by its unique identifier assigned to the construct in our lab, EPAC-S^{H201}.

Hypoxia and cyclic AMP signaling

In addition to biochemical receptor agonists such as growth factors and hormones, cells are able to sense and respond to various other environmental factors. An especially important environmental factor is the availability of molecular oxygen (O_2). Oxygen plays a vital role in the production of ATP and functions as an electron acceptor in numerous other biochemical reactions, making it an essential molecule for multicellular life[25]. Unsurprisingly, most species have evolved elaborate mechanisms for cells to adapt to differing oxygen conditions[25]. These different oxygen conditions are referred to as hypoxia (<1% O_2), often occurring in poorly vascularized tissue like solid tumors, physoxia (~5% O_2), which occurs in most normal tissues, and normoxia (20% O_2), which is the atmospheric oxygen level at which most cell biology research is performed[25–27]. The most well-studied mechanism for cellular adaptation to hypoxic conditions is the hypoxia-inducible factor (HIF) pathway. In this pathway the transcription factor HIF1α targeted for proteolytic

breakdown in an oxygen-dependent manner[28,29]. Therefore, HIF1α is not broken down in hypoxic conditions where oxygen is absent and can thus translocate to the nucleus. In the nucleus HIF1α binds to the hypoxia response element (HRE) sequence in target gene promotors, inducing the transcription of target genes involved in numerous cellular processes like cell survival, glycolysis and angiogenesis, ultimately better adapting the cell to hypoxic environment[25,30]. Additionally, increasing amounts of HIF-independent mechanisms to alter metabolism, signaling pathways and other biochemical reactions in response to hypoxia are being discovered[25,31–33]. Importantly, hypoxic conditions often occurring in solid tumors promote cancer cells to undergo further adaptations and genetic changes that allow them to survive and even proliferate, contributing to more aggressive tumor phenotypes, resistance to therapy and poor patient prognosis[25,26,30].

Since the availability of molecular oxygen has been shown to extensively influence essential cellular processes, it is to be expected there is crosstalk between hypoxia-mediated signaling and other essential regulatory signaling pathways, like the cAMP signaling pathway. Research performed over the last two decades has indeed revealed numerous hypoxia-induced changes in gene expression and protein activity of major cAMP pathway components, of which some have been shown to contribute to hypoxia-mediated cancer progression. First of all, multiple research groups report elevated levels and activity of cAMP pathway components in hypoxia, including ACs, PDEs, PKA and cAMP itself, in multiple cancer cell lines as well as in pulmonary artery muscle cells, influencing cell migration, invasion, epithelial-mesenchymal transition and angiogenesis[34–36]. Secondly, many studies report altered GPCR signaling dynamics in hypoxia, most notably the hypoxia-induced activation of GRK2 and β-arrestin, which together facilitate the desensitization of β2 adrenergic receptors[37–44]. Research has also shown that activation of the cAMP pathway by melanocortin receptor agonist α-MSH stimulates *HIF1a* gene transcription specifically in B16 murine melanoma cells[45]. Furthermore, α-MSH has been shown to have protective effects against hypoxia-mediated tissue damage *in vivo*[46]. Finally, a research group has shown upregulated CREB activity in hypoxia which leads to increased tumor growth and vascularization in carcinoma cells implanted in mice, while another group reports hypoxia-induced phosphorylation-targeted proteasomal degradation of CREB[47,48].

In conclusion, research has revealed there likely is extensive crosstalk between the response to hypoxia and cAMP signaling. However, well-described mechanisms in which hypoxia affects cAMP signaling are mostly lacking. It can be hypothesized that one contributing factor to this is the vastness of the cAMP signaling cascade, with its many (often cell-type specific) upstream activators and downstream effectors. Another contributing factor could be the limitations that are associated with performing research on hypoxia. Hypoxia is intrinsically hard to study, as exposure to atmospheric air will instantly ruin hypoxic conditions and induce reactive oxygen species in cells, which are both toxic and involved in signaling cascades[49]. As a result of this, research on hypoxia is often solely reliant on end-point assays in which no data is obtained about the precise signaling dynamics to reach that measured experimental outcome. Another issue that stems from this is that cells are often exposed to excessively high drug concentrations for long time periods, which may provide convincing end-point results, but induce unobserved adverse effects relevant to the signaling dynamics in question. Therefore, the project described in this report aims to study cAMP signaling dynamics in hypoxic conditions in real-time, utilizing the latest generation of FRET-FLIM cAMP biosensors, EPAC-S[H201], and the state-of-the-art Leica STELLARIS 8 FALCON confocal scanning microscope with ultra-fast TCSPC fluorescence lifetime detection capabilities. Since this project is very much exploratory in nature, a variety of different approaches were used, and some approaches that will be discussed remained inconclusive.

During previous work on this project, an air-tight hypoxia chamber that fits on the STELLARIS 8 microscope stage was developed, in which hypoxic conditions are reached within minutes and which allows for manipulation of cells with drugs without breaking hypoxia. Previous experiments using this hypoxia chamber have confirmed that both the mTurquoise2 donor fluorophore as well as the complete EPAC-S[H201] sensor remain functional in hypoxic conditions (Kukk *et al.*, unpublished). Over prolonged, 16 hour hypoxic exposure, the biosensor showed increased average lifetimes, which is suspected but not confirmed to be caused by elevated cAMP (Kukk *et al.*, unpublished). In this report, controls to confirm the hypoxia chamber works adequately will be performed first. Next, it will be investigated whether exposure to hypoxia influences the GPCR-mediated cAMP pathway activation, using agonists for adrenergic receptors, prostanoid receptors and melanocortin receptors in HeLa human cervical carcinoma, MelJuSo human

melanoma and B16F10 murine melanoma cell lines stably expressing EPAC-S[H201]. Furthermore, the rate at which PDEs break down cAMP in normoxic and hypoxic conditions will be investigated using an ultraviolet (UV) light-sensitive caged-cAMP variant, as well as through induction of a transient cAMP pulse by drug manipulation. Utilizing these approaches, no hypoxia-induced effects on GPCR-mediated cAMP pathway activation or cAMP breakdown by PDEs were found.

Temperature and cyclic AMP signaling

In addition to local molecular oxygen availability, extensive research efforts have been made to unravel how cells sense and respond a variety of other variables in their microenvironment. Arguably the most important microenvironmental property for proper cell functioning is temperature, as deviations from the optimal temperature (37°C for humans) can result in protein denaturing, loss of enzymatic activity and tissue damage. Therefore, multicellular organisms have evolved mechanisms by which they can sense temperature deviations and respond to them by altering blood flow, starting a protective inflammatory response or activate heat shock chaperone proteins. A well-studied mechanism by which organisms sense temperature is through temperature-sensitive members of the TRP ion channel family, each with their own temperature range[50–54]. For example, the TRPV1 channel opens up and starts a calcium influx at temperatures greater than 43°C[52–54]. Temperature-sensitive TRP channels are mostly expressed in sensory neurons, but also in epithelial cells such as in the skin[52–54]. Research highlights an important role for GPCR signaling in modulating the sensitivity of TRP channels, for example through phosphorylation by PKA and PKC downstream of GPCRs[52,53]. Although limited, research also reports that temperature changes regulate the signaling dynamics of the cAMP pathway itself[55].

Obtaining quantitative real-time data on temperature-mediated signaling dynamics using FRET sensors has historically been challenging, as focus drift due to thermal expansion can be detrimental to classical ratiometric FRET quantifications. In comparison, FRET quantification by FLIM is much less affected by focus drift[19]. Therefore, the second project described in this report aims to investigate in real-time whether and how elevated temperature affects cAMP signaling kinetics, utilizing the EPAC-S[H201] and the STELLARIS 8 confocal scanning microscope with TCSPC-FLIM capabilities. The STELLARIS 8 is outfitted with a closeable stage top incubator that allows for rapid and accurate temperature regulation. This project is also very exploratory in nature, in which a variety of different experimental approaches were used, and many remained inconclusive. First, it will be shown that elevated temperature increases biosensor lifetimes and a subsequent temperature decrease returns the lifetimes back to baseline. Control experiments using a mutated variant of the cAMP FRET-FLIM biosensor seem to confirm the effect is caused by binding of cAMP. However, this finding is contradicted by further experiments attempting to unravel mechanisms behind cause the temperature effect, which instead strongly suggest the effect is caused by a heat-induced biosensor artifact. Finally, evidence is provided that a cellular stress response might be involved in regulating the cAMP-independent lifetime increase of the cAMP FRET-FLIM sensor in response to elevated temperatures.

Results & Discussion

Hypoxia project

The hypoxia chamber and hypoxia performance controls

The goal of this project is to study signaling dynamics of the cAMP pathway in hypoxia compared to normoxia using the EPAC-S^{H201} biosensor and fluorescence lifetime imaging. To this end, a cylindrical hypoxia chamber in which gas conditions can be changed within minutes was custom designed and manufactured during previous work on this project, of which a cross-section is shown in Figure 2A. The hypoxia chamber consists of a circular aluminum base with a hole in the middle, which perfectly fits on the microscope stage insert. An exchangeable Leiden coverslip holder is inserted on top of the hole in the hypoxia chamber base, tightly fitted by a rubber O-ring for air-tight sealing and stabilization. A cylindrical aluminum body is placed on top of the base piece. The wall of the cylinder contains holes through which the controllable gas flow system, optical oxygen sensor and fluid control setup can be inserted into the hypoxia chamber. Since dry gas flows through the gas mixing system, a gas-permeable hydrophobic membrane is placed underneath the gas flow inlet, to prevent medium evaporation during experiments. The optical oxygen sensor is attached to a computer and allows for oxygen concentration measurements and logging. Finally, the fluid inlet and outlet allow for outside control of medium or buffer contents without breaking hypoxic conditions by opening the chamber. This is done by first removing buffer from the coverslip through a syringe attached to the fluid outlet tube, and subsequently adding the same volume of fresh buffer through a syringe attached to the fluid inlet tube. This fluid control system will be used to add drugs to cells in the hypoxia chamber during experiments. Additionally, the fluid inlet and outlet tubes can be closed off by a stopcock valve, which allows for multiple rounds of drug addition during a single experiment by removing the attached syringe and replacing its contents.

The fluid control system is a novel addition to the hypoxia chamber that has not been used previously. Therefore, experiments to optimize its usage have to be performed first. Since it is essential that hypoxic conditions in the chamber are not broken upon adding fresh buffer from the outside, a method to remove dissolved oxygen from the buffer prior to injecting it into the hypoxia chamber has to be developed. In order to achieve this, we attempted bubbling the bicarbonate buffer solution with nitrogen gas from the gas mixing system, which is a commonly-used deoxygenation method in chemistry. This nitrogen gas and all future referred gas mixtures also contain carbon dioxide for bicarbonate-buffered media and buffers that will be used during this project. After 5 minutes of nitrogen bubbling 15 mL buffer in an open 50 mL tube, the dissolved oxygen concentration was reduced to less than 0.3 mg/L (Figure 2B). To give more context to this value, an open 50 mL tube also containing 15 mL buffer was incubated in a hypoxic tissue culture workstation (Baker Ruskinn InvivO 2) set to 1% atmospheric oxygen. The dissolved oxygen concentration in the hypoxic workstation was measured after 24 hours, which had reduced to 0.54 mg/L, indicating that the nitrogen bubbling method allows us to efficiently reach hypoxic buffer conditions within minutes. Subsequent passive reoxygenation by contact with ambient air was relatively limited in the previously nitrogen bubbled solution in an open 50 mL tube, stabilizing around 0.9 mg/L after 6 minutes, although initial passive reoxygenation quickly rises above the value obtained in the hypoxic workstation (Figure 2B). Finally, bubbling with a gas mix containing oxygen allows for quick reoxygenation of the buffer for control experiments.

As shown, nitrogen bubbling is an efficient method to obtain hypoxic buffer for injection into the hypoxia chamber from the outside. However, the quick initial passive reoxygenation means that addition of fresh hypoxic buffer from outside of the hypoxia chamber needs to be performed as efficiently as possible. Therefore, experiments to optimize the protocol for removing and adding buffer from the outside, and to control whether hypoxic conditions remain stable during this protocol, were performed next. Prior to this experiment, 1 mL deoxygenated buffer was added onto the coverslip before quickly closing the hypoxia chamber and activating hypoxic gas flow, after which an additional 3 mL deoxygenated buffer was added into the hypoxia chamber through the fluid inlet syringe. The chamber was left like this for 15 minutes until the atmospheric oxygen level was at a minimum and dissolved oxygen was below the value previously measured in the hypoxia workstation. During these 15 minutes, five tubes containing 10 mL buffer
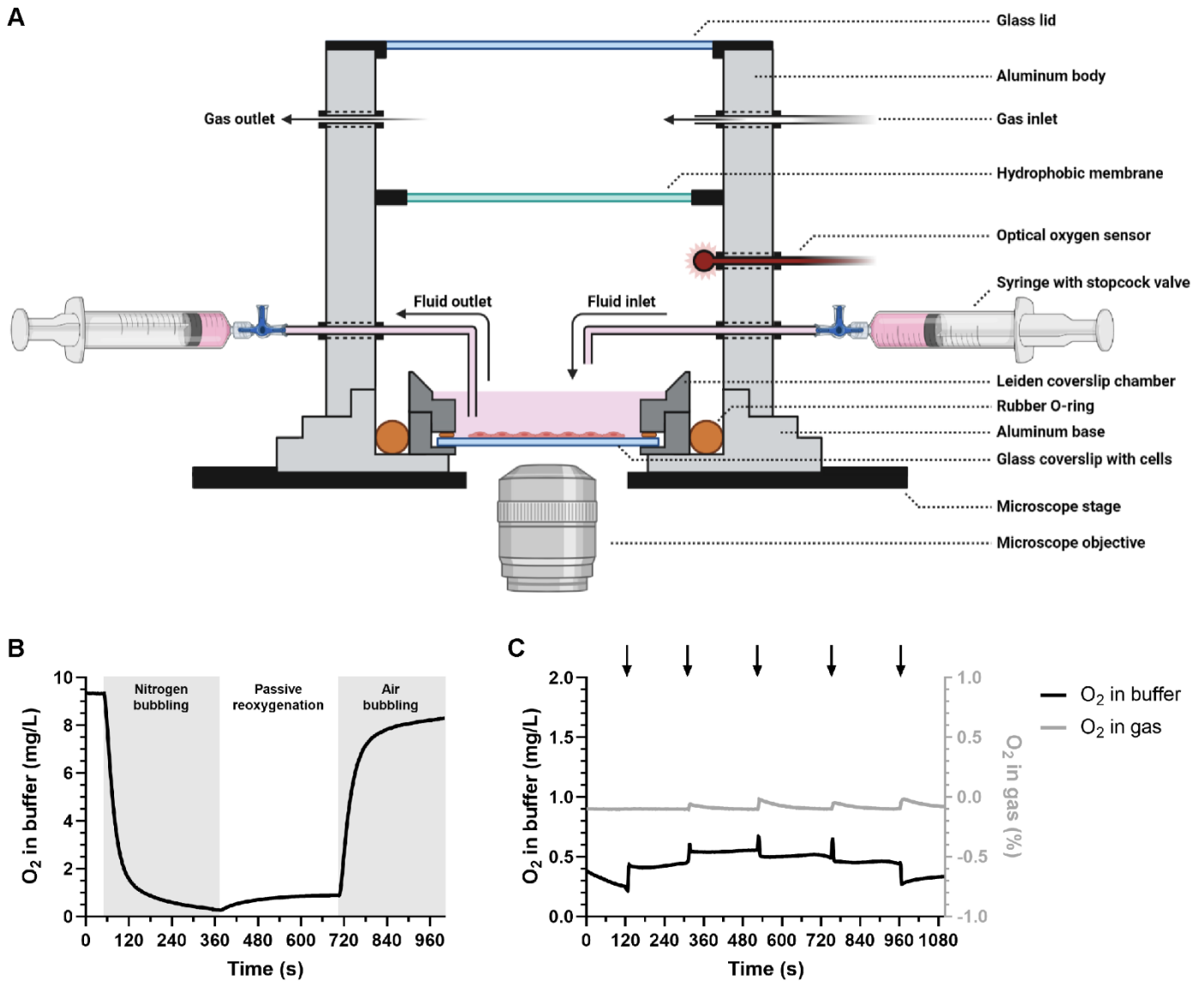
Figure 2. The custom-build hypoxia chamber and nitrogen bubbling performance tests.
(A) A schematic illustration showing a cross-section of the custom-build hypoxia chamber. The hypoxia chamber consists a circular aluminum base piece with a hole in the middle, on top of which a cylindrical aluminum body is placed. The circular base piece perfectly fits on the STELLARIS 8 microscope stage insert. A Leiden coverslip chamber is inserted above the hole in the base piece, stabilized and sealed air-tight by a rubber O-ring, allowing the objective to image the coverslip. The wall of the cylindrical body contains holes through which the gas flow system, the fluid control system, and an optical oxygen sensor can be inserted. A gas-permeable hydrophobic membrane is used to prevent medium evaporation due to the inflow of dry gas. (B) Measured dissolved oxygen concentration (mg/L) in 15 mL buffer in a 50 mL tube over time. The graph shows the effects of nitrogen bubbling, passive reoxygenation by ambient air, and air bubbling on the dissolved oxygen concentration. (C) Measured dissolved oxygen concentration (mg/L) and atmospheric oxygen concentration (%) in the hypoxia chamber over time during repeated rounds of replacing HCG buffer from inside the hypoxia chamber with freshly nitrogen bubbled buffer from outside the hypoxia chamber, using the fluid outlet and inlet system. Each round of buffer replacing is indicated by a black arrow above the graph.

solution were nitrogen bubbled for 3 minutes each and immediately closed off after. Each tube would be nitrogen bubbled for an additional 2 minutes during the experiment itself, right before being injected into the hypoxia chamber. After starting the imaging timelapse, 2.5 mL buffer was removed from the hypoxia chamber using the fluid outlet syringe and 2.5 mL deoxygenated buffer was added immediately through the fluid inlet syringe (Figure 2C). This was repeated every 2 minutes, as indicated by the black arrows for each tube respectively. While dissolved oxygen level varied slightly between different rounds of removing and adding buffer, the conditions in the chamber remained hypoxic at all times, as can be observed from the graph. Thus, we are able to change buffer conditions from outside without breaking hypoxia within the hypoxia chamber, allowing drug manipulation of cells during future experiments. Of note, the optical oxygen sensor reported negative atmospheric oxygen percentages during this experiment, which

is caused by the oxygen level in the hypoxia chamber being reduced to below the 0% calibration point of the oxygen sensor. This will also occur in some other experiments shown in this report. Finally, dissolved oxygen levels were measured through the coverslip using a second optical oxygen sensor channel during this experiment. This will not be possible in future imaging experiments because of cells plated on the coverslip and as well as the microscope objective being directly underneath the coverslip.

Hypoxia does not influence GPCR-mediated cAMP pathway activation

So far it has been shown that nitrogen bubbling is an effective method to deoxygenate buffer solutions within minutes and that it is possible to add these deoxygenated solutions into the hypoxia chamber from the outside without breaking hypoxia. The next step was to utilize this setup to evaluate whether there are differences in GPCR-mediated cAMP pathway activation under hypoxic conditions compared to normoxic conditions. Three cell lines stably expressing the EPAC-S^{H201} biosensor were imaged whilst increasing concentrations of stimulatory GPCR ligands were added onto the cells through the fluid inlet and outlet system attached to the hypoxia chamber. For each cell line the same ligand solution was used for both normoxia and hypoxia experiments, as well as a possible reoxygenated control experiment if required, in that specific order. The hypoxia experiments were performed according to the same protocol as for the experiment that was described in Figure 2C.

cAMP pathway activation in normoxic and hypoxic conditions was first investigated in HeLa EPAC-S^{H201} cells, specifically focusing on pathway activation by β adrenergic receptor agonist isoproterenol (ISO) and prostanoid receptor agonist prostaglandin E$_1$ (PGE1). Furthermore, adenylyl cyclase activator forskolin (FSK) was used as a positive control for maximum biosensor lifetime. Addition of increasing concentrations of isoproterenol caused near identical average lifetime increases in the shown representative pair of normoxia and hypoxia experiments, indicating hypoxia does not affect the cAMP pathway activation by β adrenergic receptors in HeLa EPAC-S^{H201} cells (Figure 3B). To illustrate what such an experiment looks like in microscopy images, fluorescence lifetime microscopy images of HeLa EPAC-S^{H201} cells in the normoxia experiment at different timepoints are shown (Figure 3A). These images reveal some heterogeneity in lifetime baseline and sensitivity to isoproterenol between different cells, which can be explained by this being a polyclonal cell line, with individual cells likely having slight differences in expression of key proteins involved in cAMP production and breakdown. Next, cAMP pathway stimulation by increasing concentrations of PGE1 also shows no differences in average lifetime between normoxic and hypoxic conditions, leading to the conclusion that hypoxia does not affect cAMP production by prostanoid receptors in HeLa cells (Figure 3C).

The next cell line in which cAMP pathway activation in hypoxia was investigated were MelJuSo EPAC-S^{H201} cells, again by stimulation with increasing concentrations of isoproterenol and PGE1. A difference between the average lifetime trace of the normoxia and hypoxia is observed in the shown isoproterenol experiment, in which the starting lifetime baseline of MelJuSo EPAC-S^{H201} cells in hypoxia is higher than in the normoxic condition (Figure 3D). Differences in starting baseline of this magnitude are observed more often, also between samples exposed to the same oxygen conditions. Since further differences between the normoxia and hypoxia traces can likely be attributed to the higher initial starting baseline, it is concluded that hypoxia has no effect on cAMP pathway activation by isoproterenol. In the next experiment, MelJuSo EPAC-S^{H201} cells were stimulated with increasing concentrations of PGE1 (Figure 3E). In the shown experiment it is observed that the cells seem to be more sensitive to PGE1 at higher concentration in hypoxia compared to normoxia. However, the difference observed here is again within the variability commonly observed between similar experiments in MelJuSo EPAC-S^{H201} cells, even in repeatedly performed normoxia experiments. Therefore, we conclude hypoxia has no effect on cAMP production stimulated by isoproterenol and PGE1 in MelJuSo cells.

The final cell type that was investigated for hypoxia-induced differences in GPCR stimulation are B16F10 EPAC-S^{H201} cells. B16F10 EPAC-S^{H201} cells do not express any β adrenergic receptors, and thus cannot be studied with isoproterenol. However, they do express melanocortin receptors, which were studied instead. Experiments in which melanocortin receptors were stimulated with increasing concentrations of α-MSH show melanocortin receptors seem more sensitive to α-MSH in normoxic conditions compared to hypoxic conditions (Figure 3F). However, an additional reoxygenated control experiment shows that reoxygenating the previously used hypoxic ligand solution by air bubbling
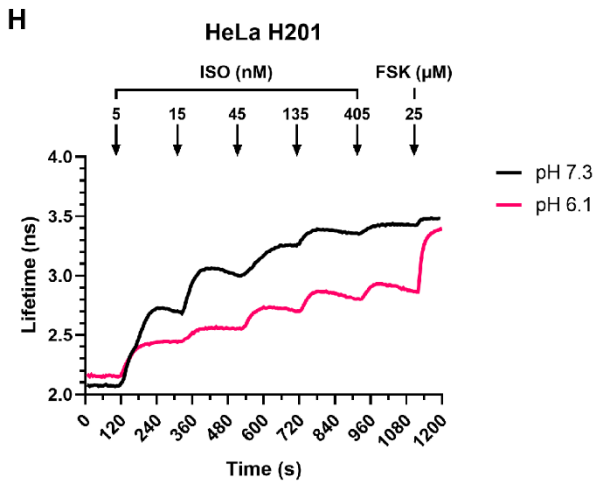
H HeLa H201
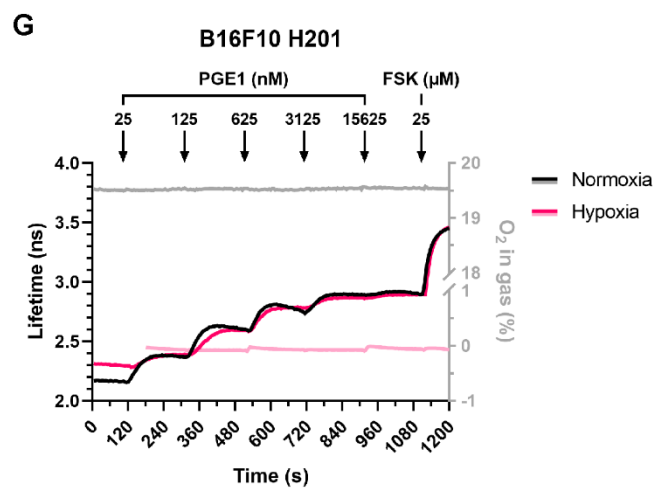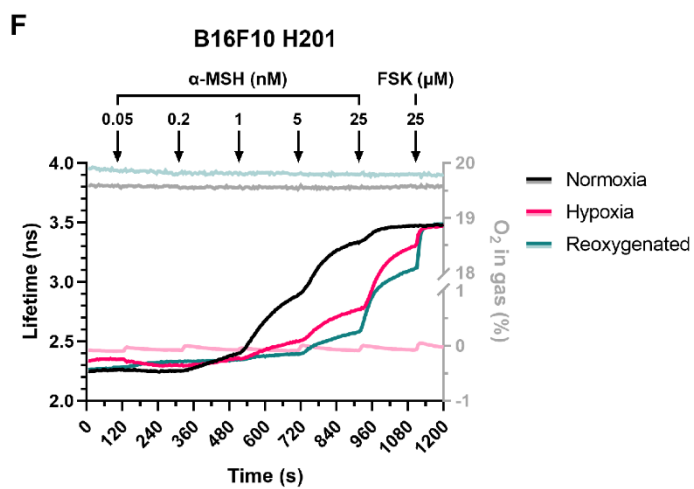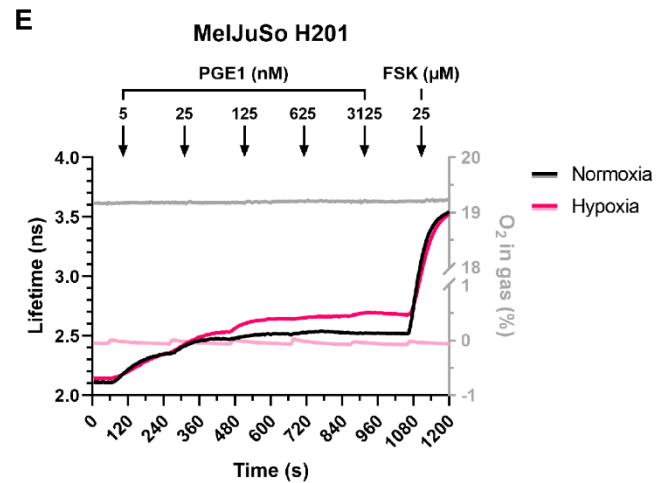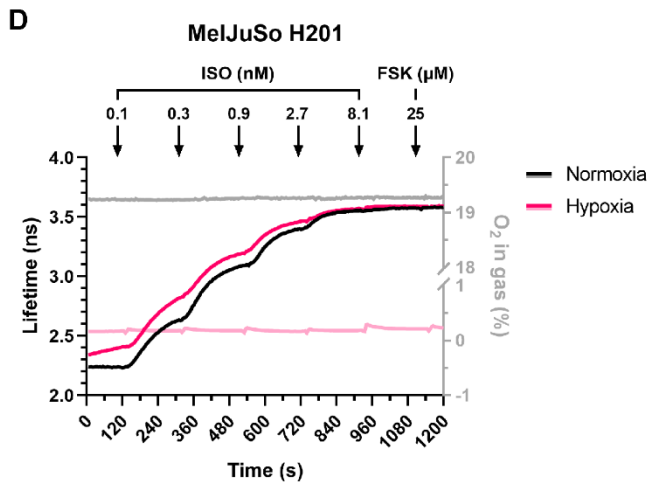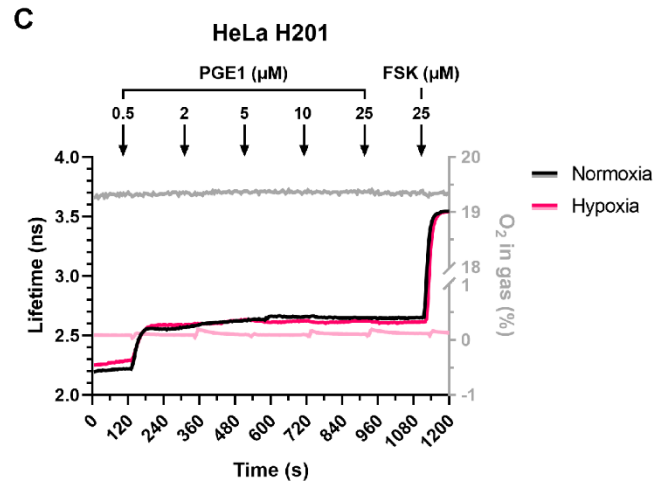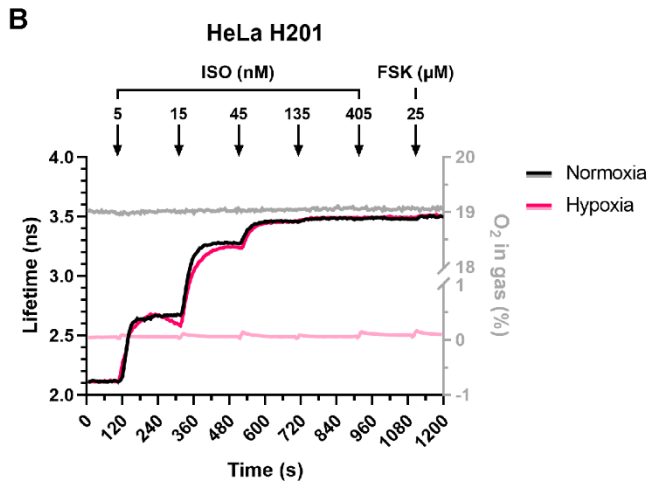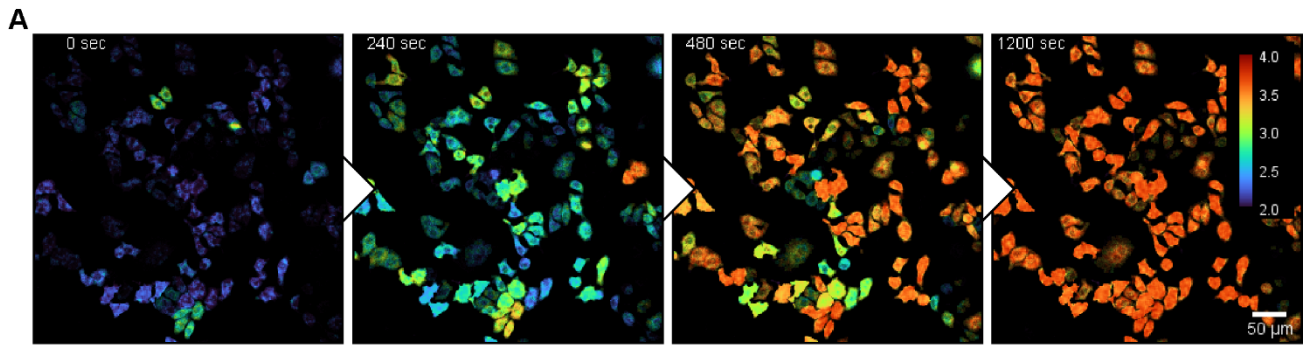
Figure 3. Studying GPCR-mediated cAMP pathway activation in normoxia vs. hypoxia by stimulating cells with increasing drug concentrations.
(A) FLIM timelapse images displaying HeLa EPAC-S[H201] cells stimulated by increasing isoproterenol concentrations. Images were obtained from the normoxia sample shown in Figure 3B. The timepoint of each image is indicated in the top-left corner. The legend in the right-most image shows the color indication used to visualize nanosecond lifetimes. (B) Whole field-of-view average lifetimes (ns) over time in HeLa EPAC-S[H201] cells stimulated with increasing concentrations of isoproterenol and forskolin in normoxia and hypoxia (n=3). Drug addition timepoints are indicated by the black arrows. Indicated concentrations represent the total concentration in the hypoxia chamber. Measured atmospheric oxygen concentration (%) in the hypoxia chamber during each experiment is indicated. (C) Whole field-of-view average lifetimes (ns) over time in HeLa EPAC-S[H201] cells stimulated with increasing concentrations of prostaglandin E_1 and forskolin in normoxia and hypoxia (n=1; normoxia n=2). (D) Whole field-of-view average lifetimes (ns) over time in MelJuSo EPAC-S[H201] cells stimulated with increasing concentrations of isoproterenol and forskolin in normoxia and hypoxia (n=1; normoxia n=2). (E) Whole field-of-view average lifetimes (ns) over time in MelJuSo EPAC-S[H201] cells stimulated with increasing concentrations of prostaglandin E_1 and forskolin in normoxia and hypoxia (n=1; normoxia n=4). (F) Whole field-of-view average lifetimes (ns) over time in B16F10 EPAC-S[H201] cells stimulated with increasing concentrations of α-melanocyte-stimulating hormone and forskolin in normoxia and hypoxia (n=3). (G) Whole field-of-view average lifetimes (ns) over time in B16F10 EPAC-S[H201] cells stimulated with increasing concentrations of prostaglandin E_1 and forskolin in normoxia and hypoxia (n=2). (H) Whole field-of-view average lifetimes (ns) over time in HeLa EPAC-S[H201] cells stimulated with increasing concentrations of isoproterenol and forskolin at pH 7.3 and pH 6.1 (n=4).

does not rescue receptor sensitivity, but instead further increases the lifetime difference compared to the original normoxic condition. This finding suggests that the agonist potency of the used α-MSH ligand solution is severely disrupted by the process of bubbling. The most likely explanation for this observation is that α-MSH peptides are possibly sticking to the walls of the polypropylene 50 mL tube in which the ligand solution is bubbled, and that this stickiness is promoted by bubbling, thereby removing α-MSH peptides from solution and lowering the concentration. Short peptides containing a mix of hydrophilic and hydrophobic amino acids have a tendency to display this stickiness, and α-MSH does fit this criterion (Figure S1)[56,57]. This also possibly explains why this bubbling-mediated loss of agonist potency has not been observed for isoproterenol and PGE1, which are both highly soluble small molecules. Thus, the observed effect on EPAC-S[H201] lifetime after α-MSH stimulation between normoxia and hypoxia is likely not caused by oxygen availability. Finally, B16F10 EPAC-S[H201] cells were also treated with increasing concentrations of PGE1 in normoxia and hypoxia, however the observed lifetime traces are identical (Figure 3G). Therefore, it is concluded that no hypoxia-induced effects on GPCR-mediated cAMP pathway activation were observed in HeLa, MelJuSo or B16F10 cells.

pH influences **β** adrenergic receptor-mediated cAMP pathway activation
Early attempts at titrating increasing drug concentrations in hypoxic conditions in the hypoxia chamber were performed with excessive levels of carbon dioxide in the gas mixture used for hypoxic gas flow in the hypoxia chamber and for nitrogen bubbling. As a result, nitrogen bubbled buffer solutions would become more acidic, with the pH dropping from 7.3 to 6.1. Interestingly, these experiments revealed a decrease in β adrenergic receptor activation by isoproterenol at acidic pH compared to physiological pH (Figure 3H). This finding is consistent with results found in literature, which shows that ligand binding by $β_2$ adrenergic receptors is greatly decreased at pH below 6.5[58,59]. Moreover, research has shown that $β_2$ adrenergic receptor activation reduces proliferation and tumor growth in breast cancer cell lines and xenografts[60]. Since the tumor microenvironment generally has an acidic pH, in some cases as low as 6.3, this finding may highlight a mechanism by which cancer cells utilize the acidic tumor microenvironment to increase cell proliferation by inhibiting $β_2$ adrenergic receptor signaling[61–63].

cAMP breakdown by PDEs under hypoxia cannot be studied with DMNB-cAMP
After finding no influence of hypoxia in GPCR-mediated cAMP pathway activation, the project moved on to test whether the activity of PDEs is influenced by oxygen availability. In order to achieve this, we used 4,5-dimethoxy-2-

11

nitrobenzyl (DMNB)-caged cAMP, a synthesized cAMP variant that can diffuse into cells and is biologically inactive until it is uncaged by UV light. A different microscope system was used for these uncaging experiments, specifically a widefield FD-FLIM system equipped with a manually toggleable UV laser, because it was not possible to uncage DMNB-caged cAMP on the STELLARIS 8. The activity of PDEs will be determined by measuring the cAMP breakdown time after uncaging by UV pulse in HeLa EPAC-S[H201] cells. An example of cAMP uncaging in HeLa EPAC-S[H201] cells is illustrated in Figure 4A, with the area targeted by the UV pulse marked by the red circle. The lifetime traces of individual cells within the FOV are shown in Figure 4B, with the black arrows indicating the uncaging events.

First, two rounds of uncaging by UV pulse were performed in normoxic conditions, after which oxygen was removed from the gas mix flowing into the hypoxia chamber. Because the cells were only covered by a small volume of 0.5 mL buffer containing DMNB-cAMP, removing dissolved and atmospheric oxygen from the hypoxia chamber happened within 15 minutes. During these 15 minutes a steady lifetime increase is observed. This increase is likely not caused by the reduced availability of molecular oxygen, as steady increasing drift in lifetime is a known recurring problem in widefield FLIM (Mukherjee *et al.*, manuscript in preparation). Next, five sequential uncaging events were performed in hypoxic conditions. The first uncaging event in hypoxia, which is the event illustrated in Figure 4A, reaches a similar lifetime amplitude as observed after uncaging in normoxia. However, in the following four uncaging events the lifetime amplitude is significantly lower. This interesting uncaging pattern in hypoxia was observed in a repeat experiment as well. Finally, reoxygenation rescues the high lifetime amplitude after uncaging.

A first hypothesis for the lower lifetime amplitudes observed after consecutive uncaging events in hypoxia is that PDEs are activated after the first cAMP pulse and that they remain activated in hypoxic conditions. The already activated PDEs then would break down cAMP as soon as it is uncaged during following uncaging events, lowering the lifetime amplitude. The possibility that PDEs remain active only in hypoxic conditions would also explain why the lower lifetime amplitudes are not observed in consecutive rounds of uncaging in normoxia. A second hypothesis for these observations however is that the uncaging reaction itself is somehow dependent on the availability of molecular oxygen, and that there was incidentally still enough molecular oxygen available in the hypoxia chamber for efficient uncaging reactions during the first UV pulse in hypoxia. This latter hypothesis is supported by the observation that the lifetime amplitude seems to become progressively lower during the experiment, as the lifetime amplitude during the second uncaging event in hypoxia is still notably higher than the following three uncaging events. More importantly, there are studies that report that molecular oxygen is involved in quenching a molecular intermediate state that obstructs the photolytic uncaging of DMNB[64,65]. This provides strong support for the hypothesis that the low lifetime amplitude observed hypoxia is caused by the absence of molecular oxygen required for the uncaging mechanism. Therefore, no conclusions about the effect of hypoxia on cAMP breakdown by PDEs can be drawn from this experiment.

An unexpected but repeatable hypoxia-induced effect was observed during the uncaging experiments. Observed only after the first uncaging event in hypoxia and only after the cells within the targeted area have already broken down the uncaged cAMP, cells outside the targeted area start displaying elevated lifetimes, as indicated by the red arrows (Figure 4AB). Since this does not occur during the normoxic conditions, it can be speculated that this observation reveals a role for cAMP signaling in cell-cell communication that, for example, promotes adaptation to hypoxia. There is evidence for the existence of such signaling in various tissues, often referred to as hypoxic preconditioning, which is mainly mediated by activation of GPCRs[66,67]. It is very much possible that secretion of GPCR ligands is also occurring during this observation, as there is a delay between the cAMP spike by uncaging in the targeted cells and the elevated lifetimes in the outermost cells. In conclusion, we have observed an effect on cellular signaling involving cAMP in HeLa EPAC-S[H201] cells that can likely be attributed to hypoxia, although precise molecular mechanisms will have to be investigated in future research.

Most graphs showing biosensor lifetime traces that have been discussed until now have depicted the average lifetime across whole field-of-view (FOV) for each timepoint, with the exception of Figure 4B, in which the lifetime trace of each individual cell in the FOV is shown. This cell-by-cell analysis was performed using a deep-learning based cell segmentation algorithm called Cellpose[68]. The combination of Cellpose with the sensitivity of FLIM and the exceptional dynamic range of the EPAC-S[H201] biosensor allows for the visualization of very subtle differences in cAMP

level on a single cell resolution. This strength is nicely highlighted by observations discussed in the previous paragraph, as the elevated lifetimes in the outermost subpopulation of cells are not nearly as visible in the whole FOV average (Figure 4B). Although the cell-by-cell method is the superior method of analysis for experiments discussed in this report, the vast majority of experiments discussed in this report will be shown as a whole FOV average, unless individual lifetime traces of those experiments contain data that is of importance to the conclusion of the experiment and project. This was done for visualization purposes, as it is nearly impossible to make a direct comparison between different conditions using individual cell lifetime traces in a single graph without compromising on the readability.
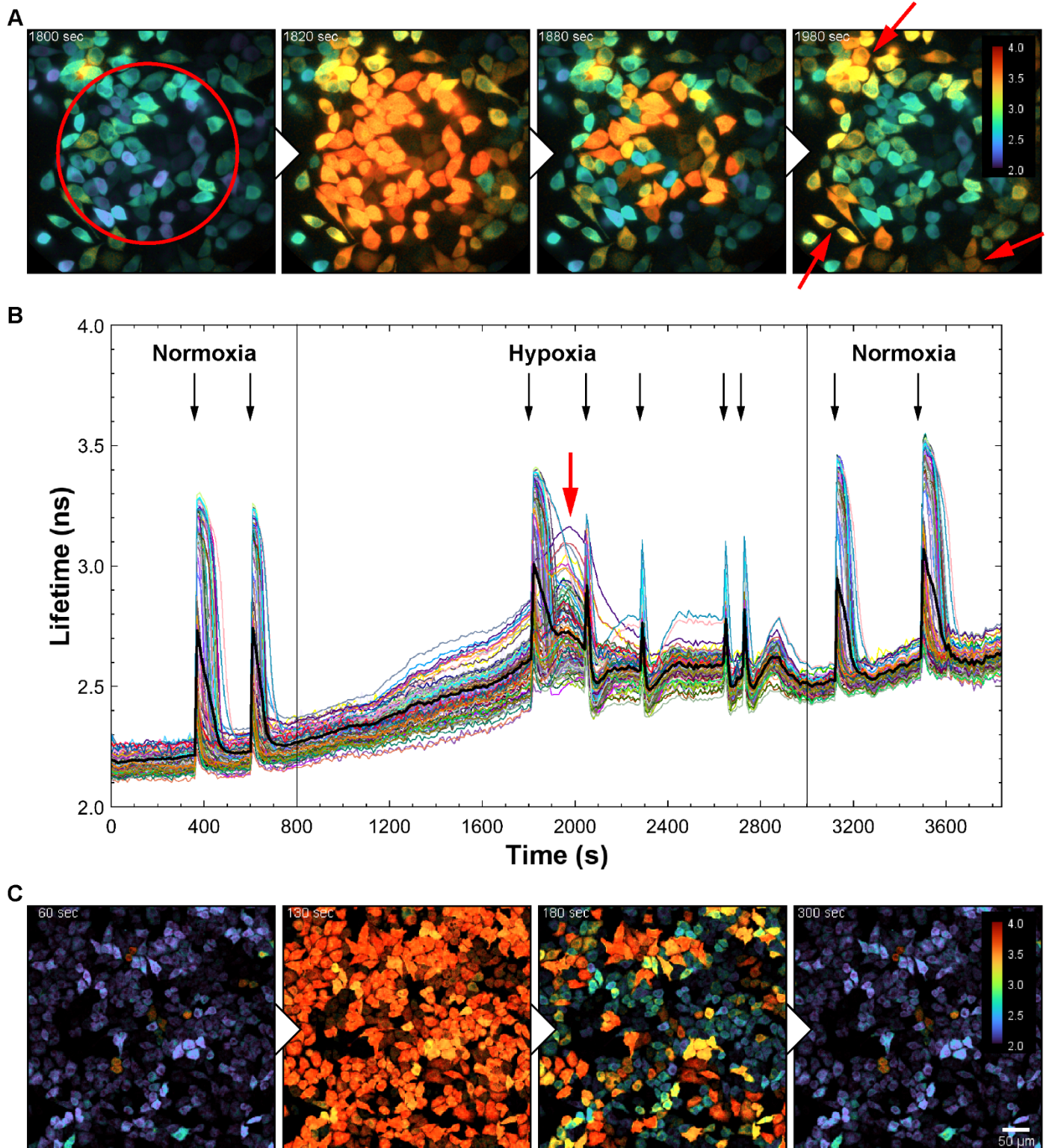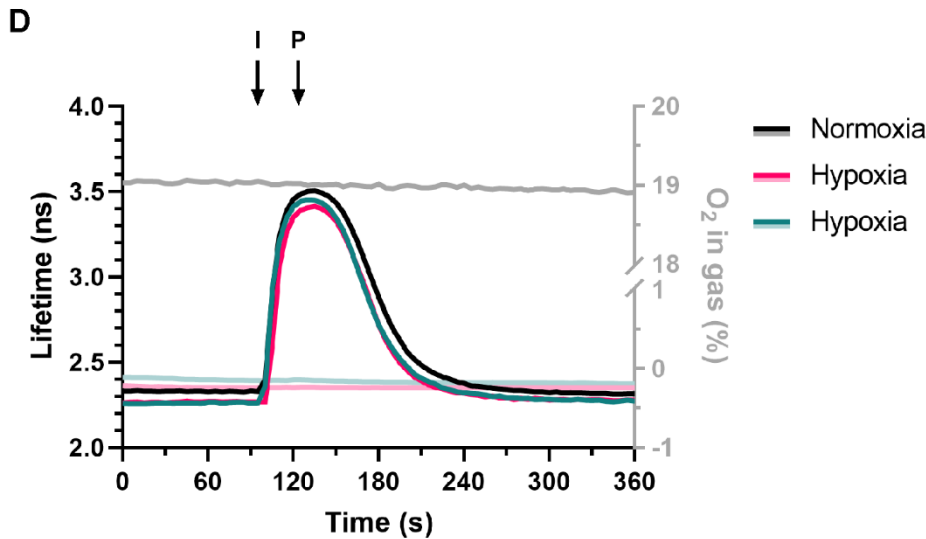
Figure 4. Studying cAMP breakdown by PDEs in normoxia vs. hypoxia.
(A) FLIM timelapse images displaying photo-release of DMNB-caged cAMP by a UV pulse and the subsequent breakdown of cAMP in HeLa EPAC-S[H201] cells. Images were obtained from the first uncaging event in hypoxia shown in Figure 4B. The area targeted by UV light is highlighted in the left-most image. The red arrows in the right-most image highlight delayed lifetime elevation in cells directly surrounding the uncaging area. The timepoint of each image is indicated in the top-left corner. The legend in the right-most image shows the color indication used to visualize nanosecond lifetimes. (B) Single cell average lifetimes (ns) over time in HeLa EPAC-S[H201] cells during repeated rounds of DMNB-cAMP uncaging in normoxia and hypoxia (n=2). Uncaging events are indicated by the black arrows. The red arrow highlights delayed lifetime elevation in cells directly surrounding the uncaging area. (C) FLIM timelapse images displaying cAMP breakdown in HeLa EPAC-S[H201] cells stimulated with 80 nM isoproterenol and 1 μM propranolol. Images were obtained from the second hypoxia sample shown in Figure 4D. The timepoint of each image is indicated in the top-left corner. The legend in the right-most image shows the color indication used to visualize nanosecond lifetimes. (D) Whole field-of-view average lifetimes (ns) over time in HeLa EPAC-S[H201] cells stimulated with 80 nM isoproterenol and 1 μM propranolol in normoxia and hypoxia (n=2). Drug addition timepoints are indicated by the black arrows. Measured atmospheric oxygen concentration (%) in the hypoxia chamber during each experiment is indicated.

Hypoxia does not influence cAMP breakdown time by PDEs

Because the influence of hypoxia on cAMP breakdown by PDEs could not be researched using DMNB-caged cAMP, another method to study cAMP breakdown time had to be used. In this method HeLa EPAC-S[H201] cells were stimulated with β adrenergic receptor agonist isoproterenol, rapidly followed by the addition of β adrenergic receptor antagonist propranolol, which displaces isoproterenol from β adrenergic receptors. This induces a transient peak in cAMP level that allows for studying the cAMP breakdown time by PDEs in normoxia and hypoxia. This assay has previously been successfully used to study the activity of individual PDEs in HeLa cells in our lab[4]. Since this assay requires sequential addition of isoproterenol and propranolol within seconds from each other, the fluid outlet tube attached to the hypoxia chamber was replaced by a second fluid inlet tube through which propranolol could be added. Following addition of isoproterenol and propranolol, identical cAMP breakdown times between normoxia and hypoxia were observed (Figure 4CD). Therefore, this experiment shows cAMP breakdown time by PDEs in HeLa EPAC-S[H201] cells is not influenced by hypoxia.

Hypoxia chamber validation experiments using common hypoxic markers remained inconclusive

The initial experiments performed to optimize and control for the performance of the hypoxia chamber and nitrogen bubbling yielded strong results, with atmospheric oxygen levels being reduced below the 0% calibration point and dissolved oxygen levels reaching a level that is lower than in a typically-used 1% oxygen hypoxia workstation. However, experiments investigating whether hypoxia influences the cAMP pathway revealed no difference in GPCR activation or cAMP breakdown. The only observed hypoxic effects were obtained from the uncaging experiments, which showed that hypoxia obscures photolytic uncaging of the DMNB cage, but also revealed potential hypoxia-induced cell-cell communication that, at present, has not been investigated further. Since there is otherwise largely a lack of findings that show a direct effect of hypoxia on the cellular biology, we attempted to perform control experiments to check whether commonly-used hypoxia biomarkers are induced by the hypoxic environment in the hypoxia chamber.

14

Firstly, a Western blot to detect hypoxic-induction of HIF1α was performed. Samples were exposed to either normoxia, various lengths of hypoxia, or normoxia in the presence of $CoCl_2$, which stabilizes HIF1α and thereby acts as a positive control. While the loading control confirms there was a sufficient amount of protein loaded into the gel, there is no staining visible at all at the expected height for HIF1α (Figure S2A). Since the positive control sample also lacks any staining, no conclusion can be drawn about whether or not the hypoxic environment in the chamber is hypoxic enough to induce HIF1α stabilization. A possible explanation for the lack of HIF1α could be that HIF1α is rapidly degraded after exposure to air during the lysis process outside of the hypoxia chamber. However, protein denaturing compounds such as β-mercaptoethanol in the lysis buffer, as well as $CoCl_2$ in the positive control sample, should prevent proteolytic breakdown of HIF1α. A final explanation is that the antibody has lost its stability and does not recognize HIF1α anymore. Since the antibody has also performed unreliably in the hands of other researchers at the institute, and was even stored at -80°C as a precaution (as opposed to -20°C suggested by the manufacturer), this is possibly the most likely explanation.

A second experiment to control whether the intracellular environment is truly hypoxic in the hypoxia chamber was performed using pimonidazole staining. Pimonidazole is a compound that undergoes a reduction reaction under hypoxic conditions. Reduced pimonidazole can then bind to macromolecules containing a thiol (-SH) group, such as proteins[69]. Therefore, pimonidazole can be used an intracellular hypoxia marker, and can be visualized using an antibody. However, in two separate experiments the pimonidazole immunostaining was not only observed in the sample exposed to hypoxic conditions, but also in the sample exposed to normoxic conditions, which can only be attributed to non-specific binding of either pimonidazole, primary or secondary antibodies (Figure S2B). Since specific immunostainings have recently been obtained using the same batch and working conditions of pimonidazole and anti-pimonidazole antibodies, non-specific binding of secondary antibodies is the most likely option[70]. Future attempts at performing this staining should include negative controls without pimonidazole, primary or secondary antibodies. In conclusion, experiments aimed at validating whether the hypoxia chamber induces intracellular hypoxic conditions have not yielded reliable results. Nevertheless, the initial oxygen concentration measurements during hypoxia chamber and nitrogen bubbling optimization indicate the hypoxia chamber performs reliably. Combined with the observation of a local hypoxia-induced cell-cell signaling effect after uncaging, we believe the combination of this custom-build hypoxia chamber with fluorescence lifetime imaging of FRET-based biosensors has been shown to be a potent asset to the current field of hypoxia research.

Temperature project

Elevated temperature increases biosensor lifetime

The aim of this second project is to research whether and how temperature changes have an influence on cAMP signaling pathway kinetics. This will be investigated mostly in HeLa cells stably expressing the EPAC-S^{H201} biosensor, primarily using the STELLARIS 8 TCSPC-FLIM confocal scanning microscope equipped with a closable stage top incubator that allows for rapid and reliable temperature regulation. Some experiments, however, were performed on a SP8 FALCON TCSPC-FLIM confocal system, the predecessor of the STELLARIS 8. The SP8 FALCON was equipped with a cage incubator that would not allow for reliably changing the temperature. Therefore, an open, heated stage insert was used to heat the Leiden coverslip holder. During all upcoming temperature regulated experiments, the temperature was measured, but not logged, by a temperature sensor that was inserted into the sample.

The first experiment performed was aimed at determining whether the cAMP level in HeLa EPAC-S^{H201} cells changes in response to increased temperature (Figure 5A). In this graph, and any future graphs visualizing biosensor lifetime and temperature over time, the colored backgrounds represent the timeframe where the heating control system was set to an increased or decreased value, and the given temperature value indicates the stabilized sample temperature at the end of that timeframe. The time required to reach a stable increased or decreased temperature depends on the total temperature change, but was generally in under 10 minutes for heating and in under 20 minutes for cooling. The results of this experiment clearly show an increased lifetime in response to elevated temperature, with the lifetime increase amplitude being higher at higher temperatures (Figure 5A). Subsequent cooling to 37°C returned the average biosensor lifetime back to baseline, and further cooling to 30°C decreased the lifetime further as well. The same effect was also observed in MelJuSo EPAC-S^{H201} and B16F10 EPAC-S^{H201} cells, as well as in African green monkey kidney fibroblast-like COS7 cells stably expressing EPAC-S^{H250} (Figure 5B). The EPAC-S^{H250} construct encodes same EPAC-S^{H201} biosensor, but is fused to a photoactivatable mCherry by a self-cleaving peptide domain. During this project, the specific sequence of a 5 minute 37°C baseline followed by 20 minute heating to 43°C as shown in Figure 5B was performed over 40 times. Student's *t*-test statistical analysis performed on data obtained from 40 comparably performed experiments confirmed the observed difference in lifetime between 37°C and 43°C is significant (n = 40, 37°C mean = 2.482 ± 0.092 ns, 43°C mean = 2.990 ± 0.125 ns, P < 0.0001).

In order to validate that the observed lifetime changes in response to temperature are in fact caused by the binding of cAMP, and not by possible temperature-mediated artifacts in biosensor conformation like denaturing or aggregation, experiments using a mutated variant of the EPAC FLIM biosensor were performed. This biosensor contains a single point mutation that results in the substitution of a hydrophilic arginine for a hydrophobic leucine (R279L) within the EPAC cAMP binding pocket, lowering the affinity for cAMP. It is clearly visible that HeLa cells transiently transfected with this non-binding biosensor display a different lifetime pattern in response to temperature compared to the regular EPAC-S^{H201} biosensor (Figure 5C). In detail, an immediate 0.2 ns drop in lifetime is observed after increasing the temperature to 43°C, after which the lifetime recovers slightly again. It is unlikely this initial drop in lifetime is caused by a conformational change within the mutated sensor, but can rather be attributed to a physical property of fluorophores, in which a higher temperature results in a shorter fluorescence lifetime[71]. The subsequent slight recovery could possibly be caused by a small amount of cAMP still binding to the mutated biosensor. An increase in lifetime is observed after cooling the sample to 30°C, which is again likely caused by the intrinsic effect that temperature has on fluorophore lifetime and not by a conformational change in the biosensor. This is also supported by the fact that it rises higher than the starting baseline, since the temperature is now lower than the temperature at baseline. Finally, adding forskolin indeed increases the lifetime of the mutated sensor slightly, confirming there is still a small amount of cAMP that is able to bind to the sensor. All in all, the finding that the mutated biosensor does not display the same lifetime kinetics as EPAC-S^{H201} suggests the large lifetime changes by EPAC-S^{H201} in response to temperature are caused by the binding of cAMP and not by a temperature-induced artifact in the biosensor.

To confirm the suspicion that the majority of lifetime deviations in response to temperature using the mutated biosensor are caused by an intrinsic temperature effect on donor fluorophore lifetime itself and not biosensor conformation, two different experiments to isolate and visualize this intrinsic effect were performed. In the first
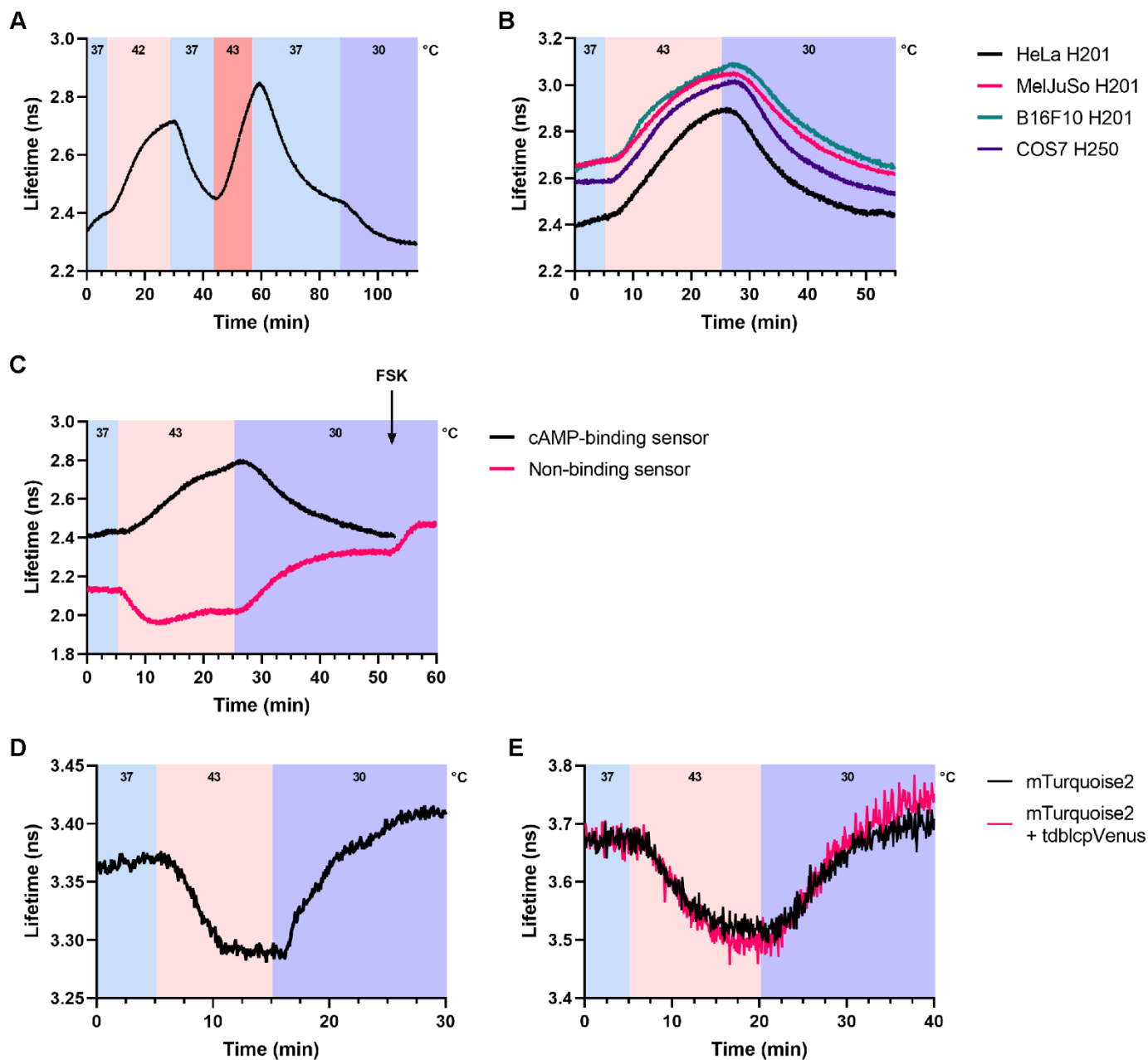
Figure 5. The effect of elevated temperature on EPAC-S^{H201} lifetime.
(A) Whole field-of-view average lifetimes (ns) over time in HeLa EPAC-S^{H201} cells exposed to different temperatures. Colored backgrounds indicate the timeframes where the temperature regulator was set to different temperatures. The indicated temperature value is the measured stable temperature at the end of each timeframe. (B) Whole field-of-view average lifetimes (ns) over time in various cell types exposed to different temperatures. (C) Whole field-of-view average lifetimes (ns) over time in either HeLa EPAC-S^{H201} cells, or wildtype HeLa cells transfected with a variant of the EPAC-S^{H201} biosensor with a mutated cAMP binding site, exposed to different temperatures (n=1). (D) Whole field-of-view average lifetimes (ns) over time in HeLa EPAC-S^{H201} cells, pre-treated with 100 μM IBMX and 250 μM forskolin to force the EPAC-S^{H201} biosensor in a cAMP-saturated low-FRET, high lifetime state, exposed to different temperatures (n=1). (E) Whole field-of-view average lifetimes (ns) over time in wildtype HeLa cells transfected with either mTurquoise2, or co-transfected with mTurquoise2 and tdblcpVenus, exposed to different temperatures (n=1).

experiment, the EPAC-S^{H201} biosensor was forced into a fully saturated state using adenylyl cyclase stimulator forskolin and PDE inhibitor IBMX (Figure 5D). As can be seen, a 6°C increase in temperature decreases the lifetime of the fully saturated sensor by about 0.2 ns, which is the same decrease that was observed in the mutated sensor. A subsequent reduction of the temperature to 30°C elevates the lifetime above the value observed at the 37°C baseline. Since the biosensor was in a saturated state during the entirety of this experiment, it can be concluded this effect is caused by an intrinsic temperature effect on fluorophore lifetime, not a conformational change in the biosensor. In the second experiment wildtype HeLa cells were transfected with only mTurquoise2 or co-transfected with both mTurquoise2 and

tdbIcpVenus. The lifetime traces in this experiment show the same pattern as observed in previous experiments, further confirming the effect is caused by a direct effect of temperature on the lifetime of the mTurquoise2 donor (Figure 5E). Interestingly, these findings also suggest that the biosensor lifetimes obtained at 43°C are underrepresented by about 0.2 ns compared to measurements at 37°C conditions, indicating that the true effect on biosensor conformation is larger than is represented by their lifetimes. In summary, the results discussed until now show a large temperature-induced increase in EPAC-S[H201] biosensor lifetime, and experiments with a cAMP non-binding variant of the EPAC biosensor suggest the temperature-induced effect on biosensor lifetime is likely caused a conformational change following the binding of cAMP.

Further attempts at revealing the cause of the heat-induced lifetime increase remained inconclusive
For this project it is essential that strong evidence about the exact cause of the increased lifetime in response to a rise in temperature is obtained. While the experiment using the mutated sensor suggests cAMP activated in response to a rise in temperature causes the lifetime increase, confirmation of these results through other experimental approaches is desired. Therefore, a number of different experiments designed to control whether cAMP is mediates the EPAC-S[H201] lifetime effect in response to a shift in temperature have been performed.

The first experiment aims to inhibit the production of cAMP by adenylyl cyclase activity by using transmembrane adenylyl cyclase inhibitor 2',5'-dideoxyadenosine (ddA). HeLa EPAC-S[H201] cells were preincubated with either 10 µM or 200 µM ddA for 1 hour before temperature experiments were performed. Results show ddA treatment did not block the heat-induced lifetime increase, suggesting that the temperature-induced lifetime effect is not caused by cAMP production by transmembrane adenylyl cyclase, instead suggesting it is caused by a biosensor artifact (Figure 6A). There are a number of other explanations for this result as well, including the possibility that adenylyl cyclase was not sufficiently inhibited by the used ddA concentration and preincubation time. Another option that deserves mentioning is the possibility that cAMP was produced by soluble adenylyl cyclase, instead of the transmembrane adenylyl cyclase family that is specifically targeted by ddA. However, according to an in-house analysis of published raw RNA sequencing datasets for all cell type used in this study respectively, the cell types in which a temperature effect on biosensor lifetime was observed do not have any expression of the sole soluble adenylyl cyclase gene (*ADCY10*) (data not shown). In order to control for successful transmembrane adenylyl cyclase inhibition by ddA, a transient cAMP spike was induced using the isoproterenol-propranolol assay in HeLa EPAC-S[H201] cells preincubated with 200 µM for 1 hour (Figure 6B). Either no cAMP spike or a reduced cAMP spike should be observed if ddA treatment successfully inhibited adenylyl cyclase, however the opposite is true. This finding shows that adenylyl cyclase is not sufficiently inhibited by this ddA treatment. Since literature indicates the EC_{50} for adenylyl cyclase inhibition by ddA is 3 µM, it is unlikely the insufficient inhibition can be attributed to the ddA concentration used in these experiments[72]. It is however possible that a 1 hour pre-incubation time is not a sufficient timeframe for adenylyl cyclase inhibition, or that the used ddA stock had lost the majority of its inhibitory potency over time in storage. In any case, these experiments could not provide any conclusions on whether the temperature effect on biosensor lifetime is caused by binding of cAMP or a temperature-related biosensor artifact.

The next set of experiments performed to investigate whether cAMP binding causes the increased biosensor lifetime in response to elevated temperature attempted to use two different ratiometric FRET biosensors for activity of PKA, a major effector protein activated by cAMP. The first PKA biosensor in question is AKAR2, which consist of a peptide sequence that can be phosphorylated exclusively by PKA. This peptide sequence is flanked by a CFP donor and YFP acceptor. AKAR2 undergoes a conformational change upon phosphorylation of the peptide sequence by PKA, which results in an increase in YFP/CFP fluorescence ratio[73,74]. Initial experiments on HeLa cells transfected with AKAR2 showed promising results, showing increased YFP/CFP fluorescence ratio and thus increased PKA activity in response to elevated temperatures (Figure 6C). However, repeat experiments failed to replicate this pattern (Figure 6D).

The same experiment was also performed using a second biosensor for PKA activity. This biosensor relies on the fact that PKA is a tetramer consisting of two regulatory subunits and two catalytic subunits. The regulatory subunits detach from the catalytic subunits upon binding of cAMP. By fusing a CFP donor fluorophore to the regulatory subunits and a YFP acceptor fluorophore to the catalytic subunits, the CFP/YFP fluorescence ratio can be used to quantify FRET

and thereby whether PKA is in its inactive tetramer state or its detached active state. Results obtained with this sensor are also inconsistent, with one trace even showing a clear decrease in active PKA. (Figure 6E).
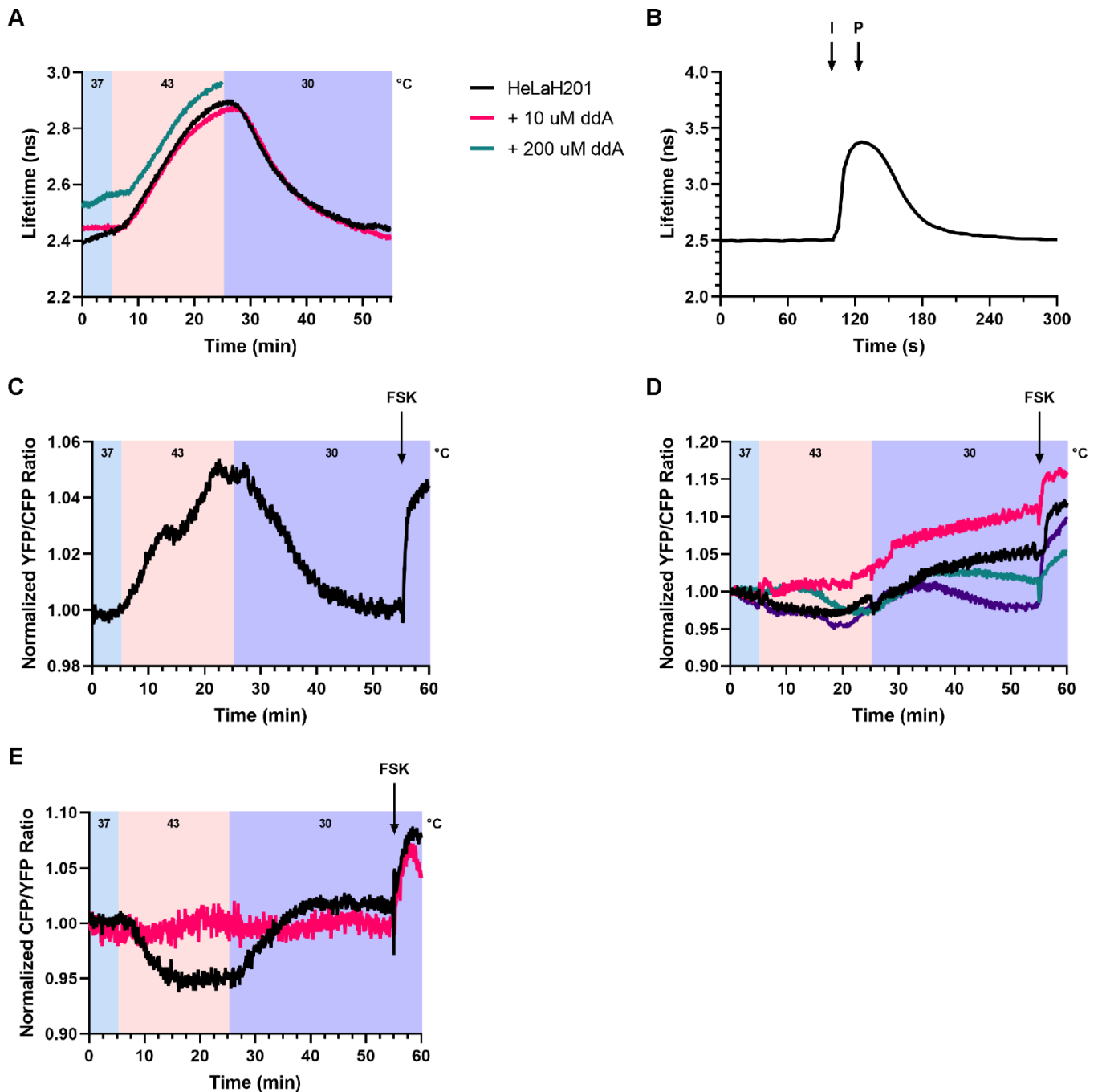

Figure 6. Inconclusive attempts at investigating whether the temperature effect is caused by cAMP.
(A) Whole field-of-view average lifetimes (ns) over time in HeLa EPAC-S[H201] cells, pre-treated with the indicated concentration of ddA for 1 hour, exposed to different temperatures (n=4). Colored backgrounds indicate the timeframes where the temperature regulator was set to different temperatures. The indicated temperature value is the measured stable temperature at the end of each timeframe. (B) Whole field-of-view average lifetimes (ns) over time in HeLa EPAC-S[H201] cells, pre-treated with 200 µM ddA for 1 hour, stimulated with 60 nM isoproterenol and 100 nM propranolol (n=1). (C) Whole field-of-view average normalized YFP / CFP fluorescence intensity ratio over time in wildtype HeLa cells transfected with the AKAR2 biosensor, exposed to different temperatures. Data was obtained in first experimental attempts using this sensor (n=2). (D) Whole field-of-view average normalized YFP / CFP fluorescence intensity ratio over time in wildtype HeLa cells transfected with the AKAR2 biosensor, exposed to different temperatures. Data was obtained from experiments attempting to replicate the response observed in Figure 6C (n=6). (E) Whole field-of-view average normalized CFP / YFP fluorescence intensity ratio over time in wildtype HeLa cells co-transfected with Regulatory-PKA-CFP and Catalytic-PKA-YFP, exposed to different temperatures (n=2).

19

Due to the inconsistent and contradictory FRET ratio traces obtained using the two PKA biosensors, no conclusions about the involvement of cAMP in the temperature effect were drawn from this experiment. A likely explanation for the inconsistent and contradictory findings is the fact that ratiometric FRET sensors are inherently sensitive to imaging artifacts like focus drift, as discussed in the introduction. If there was any PKA activation by cAMP in response to elevated temperature, the dynamic range of these sensors was likely too narrow to overcome the effects of focus drift caused by thermal expansion during temperature changes and thereby to yield reliable results. This highlights the power of FLIM over ratiometric FRET, as FLIM measurements are more resilient to focus drift, however no PKA FLIM biosensors were at our disposal at this point in time.

Stimulatory G protein knockout and cAMP ELISA experiments strongly exclude an effect of temperature on cAMP levels

After the unsuccessful attempts at obtaining proof for whether or not the temperature-induced lifetime effect is caused by binding of cAMP to the EPAC-S[H201] biosensor, a new opportunity to shed light on this question became available. For a different project that was simultaneously being researched in the lab, a monoclonal COS7 EPAC-S[H250] cell line containing a knockout of the stimulatory G protein subunit $G_{\alpha s}$ (*GNAS*) was created. Since the temperature-induced effect on biosensor lifetime had already been observed previously in COS7 EPAC-S[H250] cells, this GNAS knockout line will allow for studying whether the activation of adenylyl cyclase by $G_{\alpha s}$ to produce cAMP is involved in the observed temperature effect on biosensor lifetime. First, an experiment to functionally validate the GNAS knockout was performed. COS7 EPAC-S[H250] cells with and without the GNAS knockout were stimulated with isoproterenol (Figure 7A). Indeed, the isoproterenol-induced cAMP production was hampered in COS7 EPAC-S[H250] GNAS knockout cells compared to regular COS7 EPAC-S[H250] cells, which functionally confirms the GNAS knockout. However, a full inhibition of isoproterenol-induced cAMP production was expected. The reduced but still present lifetime increase shows that COS7 EPAC-S[H250] GNAS knockout cells possess a functionally redundant mechanism to stimulate adenylyl cyclase activity that is not dependent on $G_{\alpha s}$. A hypothesis to explain this observation is that the lesser-known $G_{\alpha olf}$, the sole other member in the G_s protein family, is expressed in COS7 EPAC-S[H250] cells and acts as a substitute for $G_{\alpha s}$ in β adrenergic receptor signaling in GNAS knockout cells. This hypothesis is backed up by data from an in-house analysis of published raw RNA sequencing datasets in wildtype COS7 cells that shows COS7 indeed do have some $G_{\alpha olf}$ expression (data not shown), as well as published studies reporting that $β_2$ adrenergic receptors can signal via $G_{\alpha olf}$[75,76].

Now that the effect of the GNAS knockout in COS7 EPAC-S[H250] cells on cAMP production by adenylyl cyclase has been validated, the next step was to expose COS7 EPAC-S[H250] and COS7 EPAC-S[H250] GNAS knockout cells to an elevated temperature. As can be clearly seen, COS7 EPAC-S[H250] cells with the GNAS knockout still displayed the temperature-induced effect on biosensor lifetime, even though cAMP production by adenylyl cyclase was shown to largely inhibited the GNAS KO (Figure 7B). This provides evidence that increased biosensor lifetime in response to elevated temperature is not caused by canonical cAMP pathway activation through $G_{\alpha s}$, but instead possibly the product of an artifact in the biosensor conformation, for example heat-induced biosensor misfolding or aggregation. There are however other hypotheses to explain this observation. For example, it is possible that adenylyl cyclase is spontaneously activated in response to elevated temperature due to a heat-induced conformational change without the need for stimulation by $G_{\alpha s}$. Another possibility is that the temperature effect is driven by the $G_{\alpha s}$-independent mechanism to activate adenylyl cyclase observed in Figure 7A, for example by $G_{\alpha olf}$. For this latter hypothesis to be true, the $G_{\alpha s}$-independent mechanism would have to be aided by a decrease in cAMP breakdown activity by PDEs at elevated temperature, since the $G_{\alpha s}$-independent lifetime increase in isoproterenol-stimulated GNAS knockout cells is quite a bit lower than the observed heat-induced lifetime increase in Figure 7B. Prior to obtaining the results with the COS7 EPAC-S[H250] GNAS knockout cells, an experiment investigating the activity of PDEs at different temperatures in HeLa EPAC-S[H201] cells had already been performed. In this experiment, the isoproterenol-propranolol assay was performed on HeLa EPAC-S[H201] cells at different temperatures (Figure 7C). The results showed there is no difference in PDE activity at 42°C compared to 37°C, only a decrease at lower temperatures, likely because the low temperature is outside the optimal temperature range for proper enzymatic functioning. Therefore, the most likely hypothesis for

the temperature effect is either caused by heat-induced artifact in biosensor conformation, or by spontaneous heat-induced adenylyl cyclase activation.
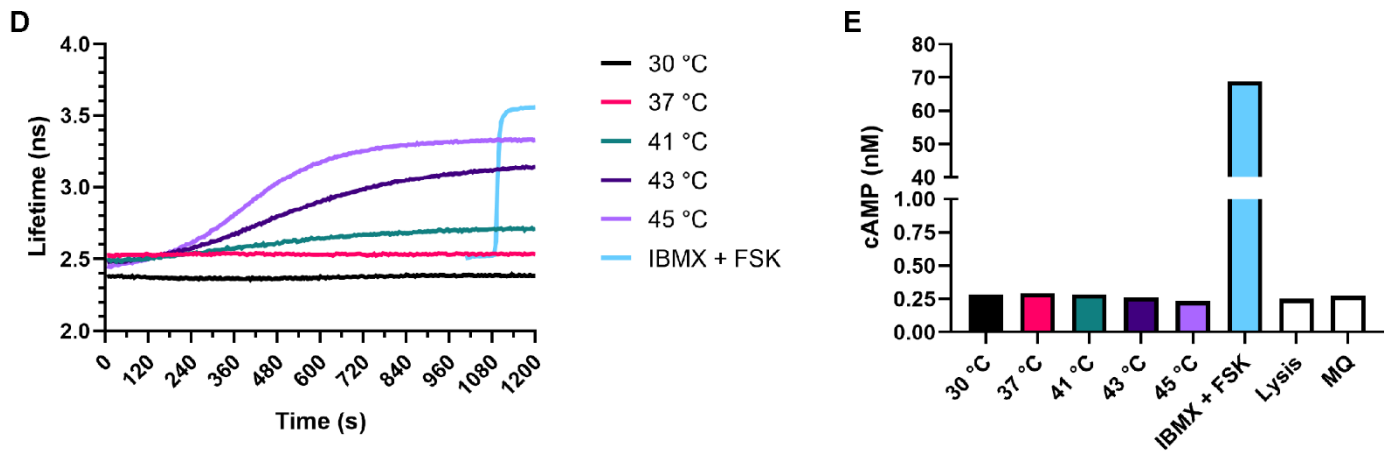
A

B

C
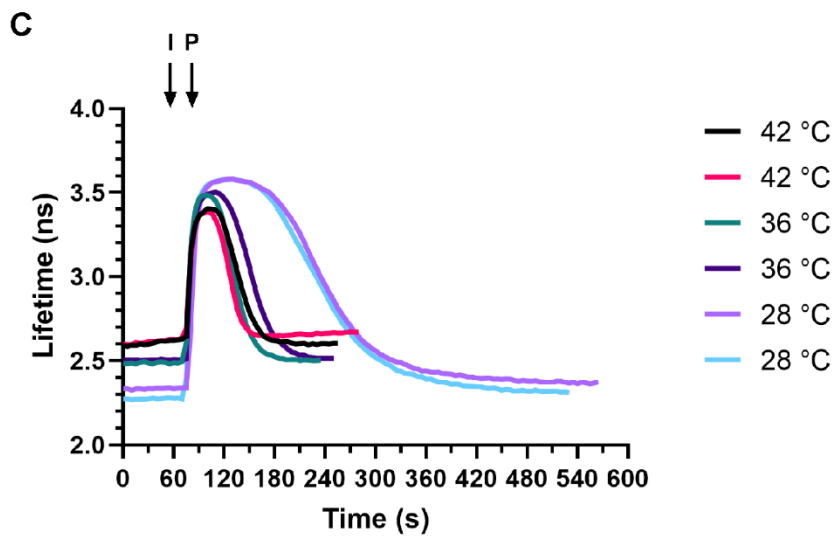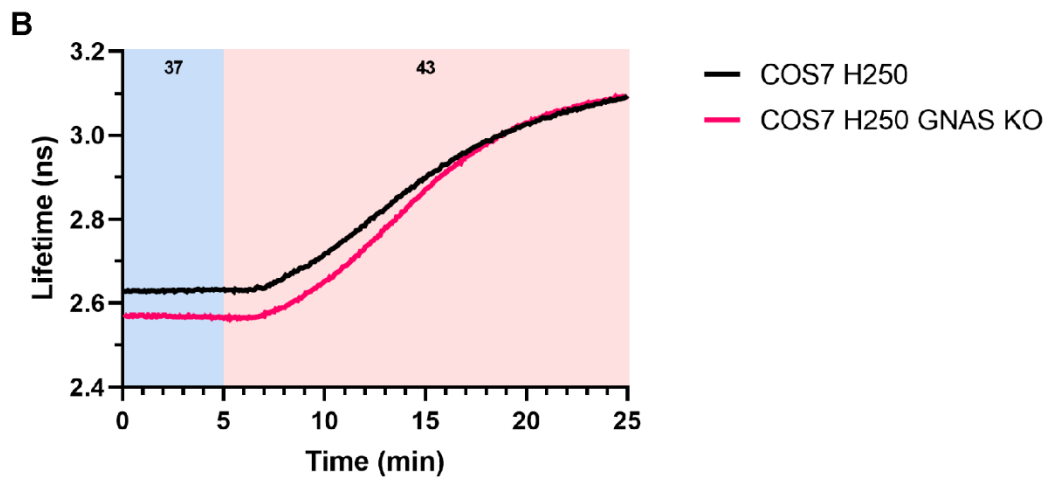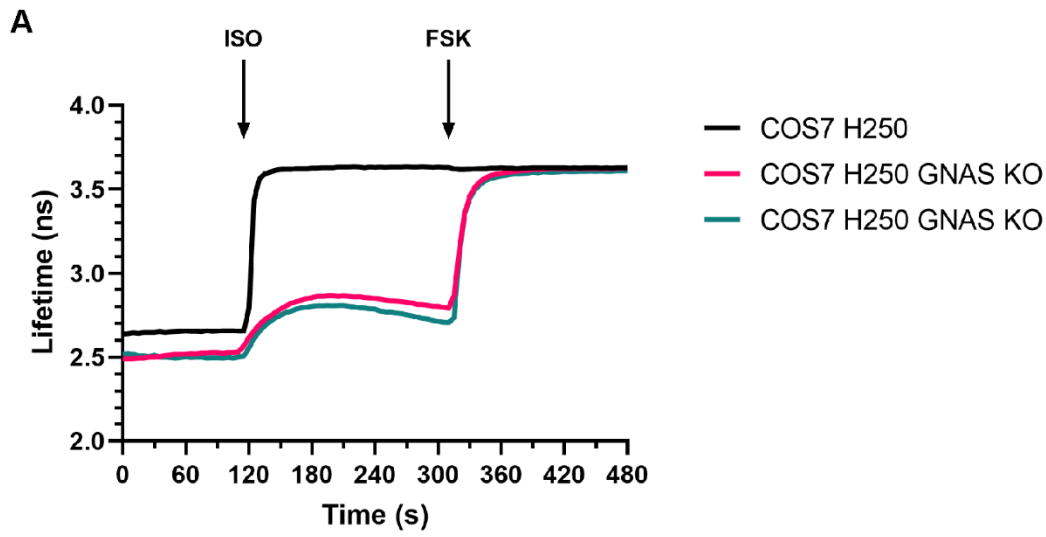
Figure 7. Stimulatory G protein knockouts and an enzyme-linked immunoassay show cAMP is not is involved in the heat-induced EPAC-S[H201] lifetime increase.

(A) Whole field-of-view average lifetimes (ns) over time in COS7 EPAC-S[H250] cells with and without the *GNAS* knockout, stimulated by 40 nM isoproterenol and 250 μM forskolin to functionally validate the *GNAS* KO (n=2). Drug addition timepoints are indicated by the black arrows. (B) Whole field-of-view average lifetimes (ns) over time in COS7 EPAC-S[H250] cells with and without the *GNAS* knockout, exposed to different temperatures (n=1). Colored backgrounds indicate the timeframes where the temperature regulator was set to different temperatures. The indicated temperature value is the measured stable temperature at the end of each timeframe. (C) Whole field-of-view average lifetimes (ns) over time in HeLa EPAC-S[H201] cells stimulated with 60 nM isoproterenol and 100 nM propranolol at different temperatures (n=2). Drug addition timepoints are indicated by the black arrows. (D) Whole field-of-view average lifetimes (ns) over time in HeLa EPAC-S[H201] cells at different temperatures, as well as a control sample treated with 100 μM IBMX and 250 μM forskolin. Samples were lysed at the end of the timelapses and lysates were used for the cAMP ELISA shown in Figure 7E. (E) Extrapolated cAMP concentrations in the ELISA reaction volume for each sample that was lysed at the end of the timelapses in Figure 7D. Two background controls where performed, in which sample lysate was substituted for lysis buffer or Milli-Q.

Finally, in order to confirm which one of these two hypothesis is true, an enzyme-linked immunosorbent essay (ELISA) to detect cAMP concentrations was performed on cell lysates from samples that were exposed to differing temperatures. Figure 7D shows the average lifetime traces for all samples used in this experiment, including a positive control treated with IBMX and forskolin, with samples being lysed on ice immediately after the end of the imaging timelapse at 20 minutes. cAMP concentrations in the lysates were extrapolated from an absorbance standard curve based on a series of known cAMP concentrations ($R^2 = 0.98$). The extrapolated cAMP concentrations in all samples exposed to different temperatures were the same as in the two background controls, in which no cell lysate was added but substituted by the same volume of either lysis buffer or Milli-Q (Figure 7E). Therefore, these extrapolated concentrations are background noise, so no cAMP was present in the cell lysates. This finding provides strong support for the hypothesis that the temperature-induced lifetime effect is not caused by cAMP, but instead by a heat-induced artifact in the conformation of the biosensor. We believe these results to be reliable for a number of reasons. First of all, in previous instances where this cAMP ELISA kit was used in the lab, spike controls (i.e. adding a known cAMP concentration to a cell lysate) returned the expected concentrations, indicating that the enzyme-linked immunoassay is accurate and reliable (Kukk *et al.*, unpublished). Furthermore, the positive control cAMP concentrations in this ELISA are similar to that in the same control conditions during previous experiments using this kit (Kukk *et al.*, unpublished). Since the PDE inhibitor IBMX was not added to the lysis buffer, an argument can be made for the potential breakdown of cAMP during the lysis process, which could explain why cAMP is only detected in the sole condition treated with IBMX. However, previously performed control experiments showed no effect of adding IBMX to the lysis buffer on cAMP concentration (Kukk *et al.*, unpublished). Furthermore, the coverslips were placed directly on ice within seconds after taking them out of the stage top incubator on the STELLARIS 8, and the entire subsequent lysis process was performed on ice, it is highly unlikely a significant amount of cAMP could have been broken down by PDEs. Finally, the lysis buffer contains Triton X-100, which destabilizes proteins like PDEs.

In summary, numerous different experiments have been performed to investigate whether the temperature effect was caused by binding of cAMP to EPAC-S[H201], or by a heat-induced biosensor artifact. While initial experiments using a low cAMP affinity mutated biosensor suggested binding of cAMP to the biosensor is the cause of the temperature effect, this finding was contradicted by COS7 GNAS knockout cell experiments and cAMP ELISA experiments. Since the latter two provide especially strong evidence for the hypothesis that the effect is caused by a cAMP-independent heat-induced conformational change in the EPAC-S[H201] biosensor, we conclude the EPAC-S[H201] cannot be used to study cAMP signaling dynamics at elevated temperatures.

Cellular stress coping mechanisms seem to have an effect on the heat-induced biosensor lifetime increases

The elevated temperature experiments that that have been discussed in this report so far have shown a transient heat-induced effect on biosensor lifetime, in which the lifetime increases in response to elevated temperature and decreases again in response to lowered temperature. However, during some initial experiments testing the stage insert heating system on the SP8 FALCON, some samples were heated to over 43°C, which was the maximum temperature used during the other experiments in this project. Interestingly, samples heated above 43°C often displayed a sustained increased lifetime effect after cooling, instead of a transient one (Figure 8A). Attempts to replicate these sustained long lifetimes using the closed stage top incubator on the STELLARIS 8 were successful, showing similar sustained responses at temperatures staring at 45°C (Figure 8B). This observation suggests there is a thermal threshold, or a cellular response mechanism to excessively high temperatures, in which the EPAC-S[H201] biosensor in retained in a heat-induced long lifetime state.

In an attempt to investigate whether or not cells displaying sustained high lifetime responses do eventually return back to baseline lifetime, HeLa EPAC-S[H201] cells subjected to a 45°C heat shock were subsequently imaged overnight (Figure 8C). A sustained long lifetime state was successfully induced, with the average lifetime even rising an additional 0.2 ns after cooling to 37°C, which can be attributed to the intrinsic effect temperature has on mTurquoise2 lifetime. The overnight imaging revealed that cells did survive the 45°C heat shock, and that most cells returned to baseline lifetime within 12 hours. More interestingly however, it was observed that these heat-shocked cells entered a state in which some kind of stress-induced bodies enriched with the EPAC-S[H201] biosensor appeared, as is visible in the mTurquoise2 intensity image at 360 minutes and highlighted in the accompanying zoom-in (Figure 8D). General intensity differences between the four timelapse images can be attributed to mTurquoise2 fluorescence not being quenched by FRET with the acceptor fluorophore when the biosensor is in its low FRET, long lifetime conformation. The appearance of these stress bodies is in line with published studies, which have reported that stress-induced granule formation occurs at 45°C[77]. Over time the biosensor-enriched bodies disappear, specifically between hours 6 and 11 in the timelapse, coinciding with most cells returning to baseline lifetime. The formation of these biosensor-enriched bodies after exposure to high temperatures could possibly further reinforce the hypothesis that the EPAC-S[H201] biosensor misfolds or aggregates at high temperatures.

The appearance of these stress bodies was also observed in HeLa EPAC-S[H201] cells that were subjected to repeated rounds of heating to 43°C and subsequent cooling to 37°C overnight (Figure 8EF). The single cell lifetime traces show a lot of heterogeneity in lifetime between different cells at the end of this timelapse, with the average lifetime in some cells being reduced back to baseline, while other show sustained long lifetimes (Figure 8E). The FLIM images from the end of this timelapse reveal that there is a clear correlation between cells displaying an increased lifetime and the presence of fluorescent stress bodies, while none are observed in cells with a short lifetime (Figure 8F). Finally, the exact same sample from the last experiment was subjected to another round of temperature increase to 43°C the next morning (Figure 8G). In this kymograph-like image, each horizontal line of pixels represents the average biosensor lifetime of a single cell for each frame during the timelapse. It reveals there is a clear distinction between a subpopulation of cells (~10%) that show a sustained high lifetime response, and the remaining population of cells that quickly return to baseline lifetime. This final observation, together with the observed presence of biosensor-enriched bodies specifically in cells displaying sustained high lifetimes, shows that a cellular heat stress coping mechanism is actively involved in mediating the cAMP-independent heat-induced lifetime increase observed in the EPAC-S[H201] biosensor, and that the formation of stress bodies likely plays a role in this stress coping mechanism.
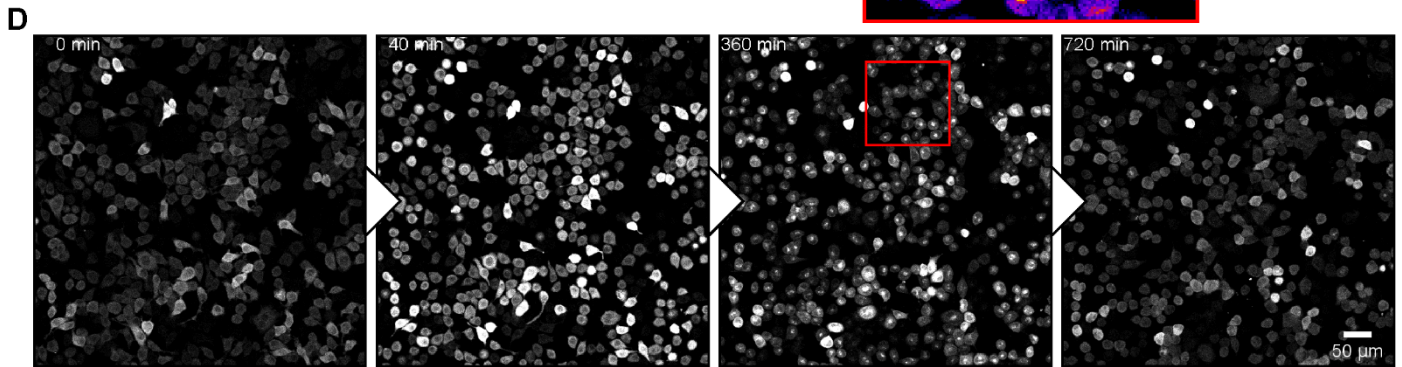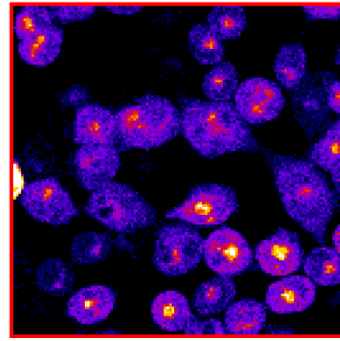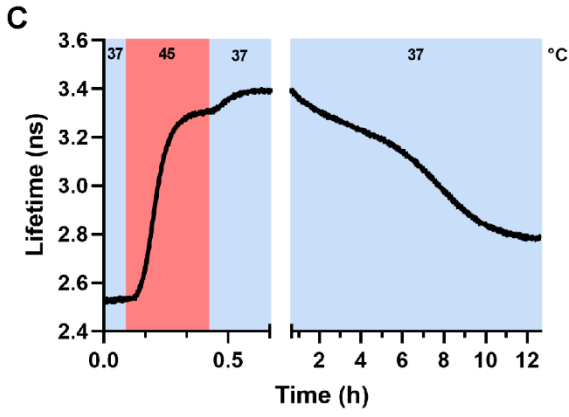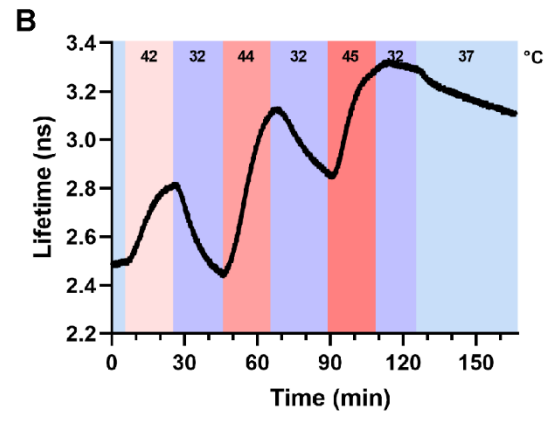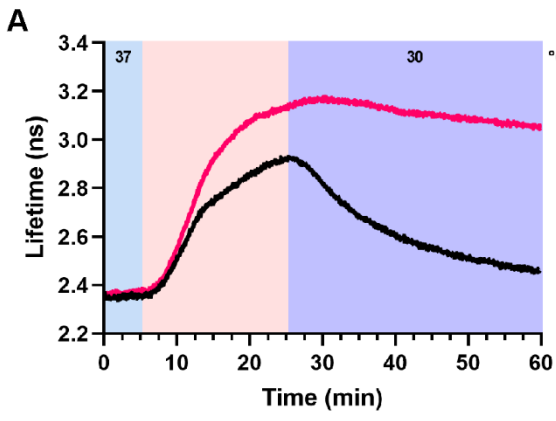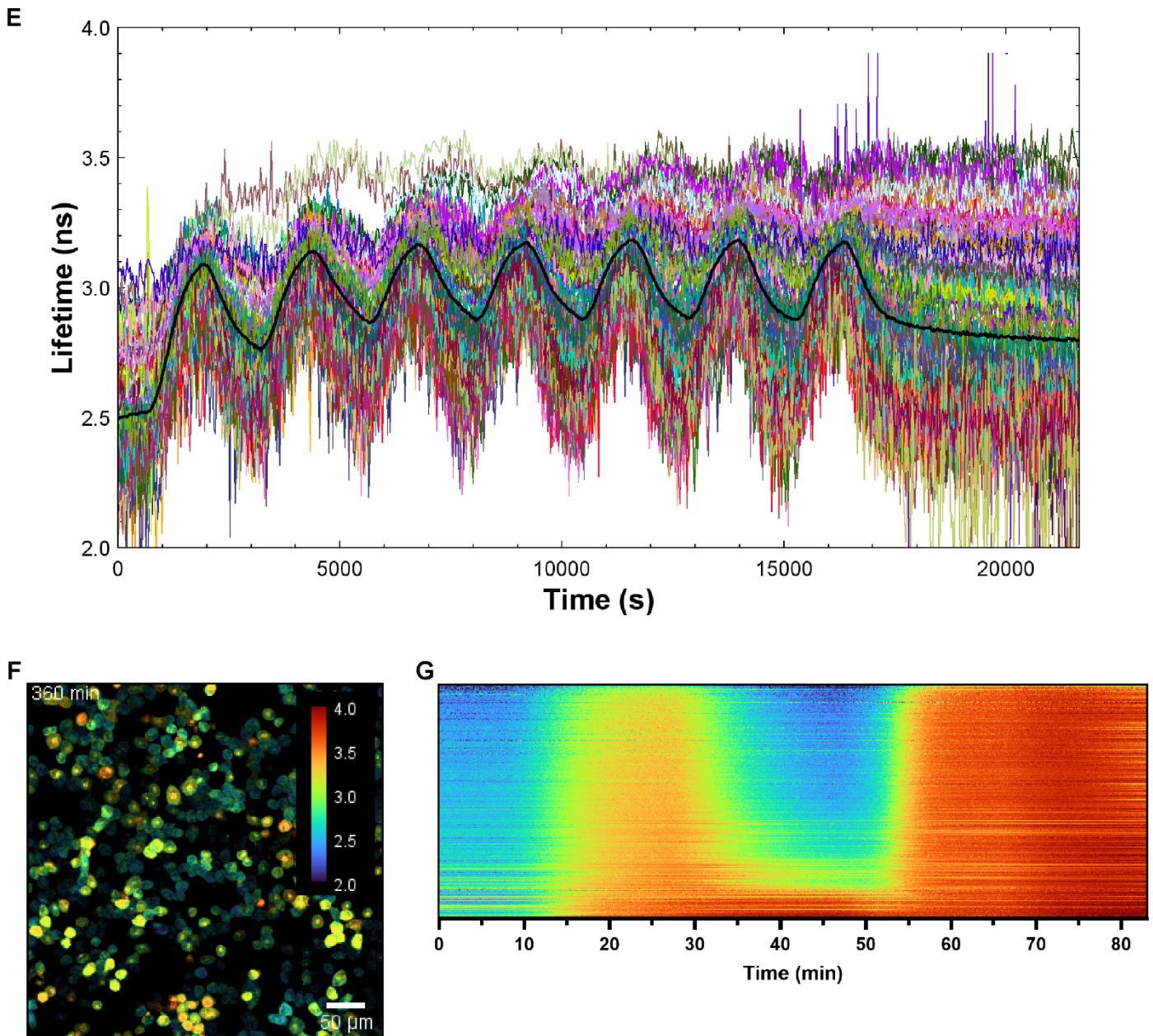
Figure 8. A cellular stress response is involved in sustained heat-induced EPAC-S[H201] lifetime increases.
(A) Whole field-of-view average lifetimes (ns) over time in HeLa EPAC-S[H201] cells exposed to 43°C or 44°C. Colored backgrounds indicate the timeframes where the temperature regulator was set to different temperatures. The indicated temperature value is the measured stable temperature at the end of each timeframe. (B) Whole field-of-view average lifetimes (ns) over time in HeLa EPAC-S[H201] cells exposed to sequential temperature increases. (C) Whole field-of-view average lifetimes (ns) over time in HeLa EPAC-S[H201] cells exposed to an excessively high temperature of 45°C. Lifetime recovery was followed in an overnight timelapse. (D) mTurquoise2 intensity images of HeLa EPAC-S[H201] cells obtained during the overnight timelapse in Figure 8C. Biosensor-enriched bodies can be observed in the third image, as clearly visualized by the zoom-in and highlighted by the 'Fire' LUT. The timepoint of each image is indicated in the top-left corner. (E) Single cell average lifetimes (ns) over time in HeLa EPAC-S[H201] cells exposed to repeated rounds of heating to 43°C and cooling to 37°C overnight. (F) A FLIM timelapse image displaying HeLa EPAC-S[H201] cells at the end of the timelapse shown in Figure 8E. Biosensor-enriched bodies are again observed, exclusively in cells displaying sustained high lifetimes. (G) A kymograph-like graph in which each horizontal line of pixels represents the average biosensor lifetime of a single cell over time in the timelapse. Data is obtained from an additional experiment performed on the exact same sample shown in Figures 8E and 8F, in which the sample was first exposed to 43°C, later followed by 45°C. Two populations with clearly distinct heat-induced high lifetime responses are observed.

25

Conclusions & Future Prospects

Hypoxia project

This project aimed to study the effect of hypoxic conditions on GPCR-mediated cAMP pathway activation and PDE-mediated cAMP breakdown in real-time using the EPAC-S^{H201} cAMP biosensor, state-of-the-art STELLARIS 8 confocal scanning microscope with FLIM capabilities and a custom-build stage top hypoxia chamber. To do so, a method to externally control drug concentrations in the hypoxia chamber without breaking hypoxic conditions was developed. It was shown that deoxygenated drug solutions can efficiently be obtained by nitrogen bubbling and that these deoxygenated solutions can be injected into the hypoxia chamber without breaking hypoxic conditions. This system was used to evaluate the influence of hypoxia on cAMP pathway activation by adrenergic, prostanoid and melanocortin receptors in HeLa, MelJuSo and B16F10 cells stably expressing EPAC-S^{H201}, by stimulating them with increasing concentrations of the respective receptor agonists. In these experiments, no differences in GPCR-mediated cAMP pathway activation between normoxic and hypoxic conditions were observed, although experiments stimulating melanocortin receptors remained inconclusive due to loss of agonist potency during the nitrogen bubbling process. Next, the cAMP breakdown by PDEs in normoxic and hypoxic conditions was studied using a biologically inactive DMNB-caged cAMP variant that can be uncaged using UV light. While the observed cAMP breakdown kinetics were different between normoxic and hypoxic conditions, it was ultimately concluded this was caused by the uncaging mechanism being disrupted in hypoxia due to its dependency on the molecular oxygen. Despite that, a hypoxia-induced cell-cell signaling effect was observed in cells surrounding the UV-pulsed area, which has not yet been researched further. Additional attempts at studying cAMP breakdown by PDEs using an isoproterenol-propranolol assay revealed no difference in cAMP breakdown time between normoxic and hypoxic conditions. Since no hypoxia-induced effects on GPCR-mediated cAMP pathway activation and PDE-mediated cAMP breakdown were observed, Western blots for HIF1α and immunostainings for pimonidazole were performed in order to confirm that the hypoxic environment in the hypoxia chamber does induce intracellular hypoxia. However, these experiments remained inconclusive because positive and negative controls respectively did not show the expected results. Despite these last controls remaining inconclusive, the oxygen measurements during hypoxia chamber and nitrogen bubbling optimization experiments strongly suggested the system is reliable. Combining those initial measurements with the observation of local hypoxia-induced cell-cell signaling effect after uncaging, we believe that the combination of this custom-build hypoxia chamber, real-time fluorescence lifetime imaging of dynamic biosensors, and single-cell analysis has been proven to be an asset the field of hypoxia research.

Longer exposure to hypoxic conditions prior to experiments
The addition of the fluid control system to the hypoxia chamber in combination with nitrogen bubbling resulted in the ability to reach hypoxic solution conditions in the chamber within minutes, as well as the ability to control drug contents within the hypoxia chamber from the outside. This has allowed us to investigate whether the availability of molecular oxygen has a direct effect on cAMP pathway activation and breakdown kinetics, although ultimately no such effects were found. Since adaptation to hypoxia induced by HIF1α relies on transcriptional rewiring, any HIF1α-dependent changes to cAMP signaling dynamics in hypoxia would not have been observable in the experiments discussed in this report, in which cells were only exposed to short-term hypoxic conditions. Previous work on this (prior to the availability of the fluid control system) has already shown that the hypoxia chamber is suited for exposing cells to long-term hypoxia, and elevated EPAC-S^{H201} average lifetimes have been observed after prolonged periods hypoxia of over 16 hours (Kukk *et al.*, unpublished). Therefore, the drug titration experiments should be repeated on cells exposed to longer periods of hypoxia, aiming to study the potential HIF1α-dependent effects hypoxia has on the cAMP signaling pathway. In combination with the already researched direct effect of molecular oxygen availability on cAMP pathway activation and breakdown, this study could provide a more complete insight into the effects of hypoxia on cAMP signaling.

Preventing loss of **α-MSH** during the bubbling process

Experiments aimed to investigate whether hypoxia influences cAMP pathway activation by melanocortin receptors remained inconclusive, due to the loss of α-MSH agonist potency that is mediated by the bubbling process. We suspect this is caused by α-MSH peptides sticking to the walls of the polypropylene 50 mL tubes in which drug solutions are bubbled, and that the bubbling process promotes this loss of dissolved α-MSH. Use of bovine serum albumin (BSA) is a commonly used method to limit proteins sticking to plastic and glass, so it may be worthwhile to repeat these α-MSH titration experiments in presence of BSA[78,79]. However, high concentrations of BSA are known to interfere with plasma membrane-localized processes like cAMP pathway activation, as well as serum albumins functioning as carriers for growth factors that signal through the cAMP pathway, like lysophosphatidic acid[80,81]. Therefore, it is recommended to not add BSA directly to the α-MSH dilutions that will be bubbled and used to study cAMP activation, but instead coat the 50 mL plastic tubes with BSA followed by washing prior to making and bubbling the α-MSH dilutions[78,79]. This should limit loss of α-MSH by sticking to the plastic, and keep the amount of BSA that potentially interferes with the experiment at a minimum.

Investigating the hypoxia-induced cell-cell communication observed after a cAMP pulse

During the experiments attempting to investigate potential effects of hypoxia on cAMP breakdown time utilizing DMNB-caged cAMP, an unexpected but interesting hypoxia-induced effect was observed in which cells directly surrounding the UV-targeted area started producing cAMP right after the cells within the UV-targeted area had broken down the uncaged cAMP. Since literature provided strong evidence that the DMNB uncaging is dependent on molecular oxygen, we hypothesized that the conditions during the uncaging event after which this effect was observed were only mildly hypoxic[64,65]. Furthermore, the slight delay between cAMP breakdown in cells within the UV-targeted area and cAMP production in the surrounding cells can suggest the effect is caused by GPCR ligand secretion by cells experiencing a cAMP pulse in mild hypoxic conditions. This suspected ligand secretion under mild hypoxic conditions appears similar to a widely reported adaptive mechanism to prevent tissue damage due to hypoxia, referred to as hypoxic preconditioning[66,67]. GPCR activation during brief hypoxia is believed to be the main mediator of this hypoxic preconditioning, with there being a number of different GPCR families whose activation has been shown to be causal for hypoxic preconditioning. This includes but is not limited to adenosine, bradykinin, opioid and urocortin receptors, as well as the adrenergic and prostanoid receptors previously mentioned in this report[66,67]. Due to the similarities with the known signaling pathways that mediate hypoxic preconditioning, it can be hypothesized the hypoxia-induced effect we observe is involved in mediating hypoxic preconditioning, warranting further research into this effect.

First experiments looking into the hypoxia-induced cell-cell communication effect should aim to confirm the effect is caused by GPCR ligand secretion. To this end, it may be efficient to first optimize reproducing the mild hypoxic conditions that still allow for DMNB uncaging, so the effect could potentially be induced multiple times in a single continuous experiment. While it would require slight modifications to the hypoxia chamber design, inducing a laminar flow in the fluid in the hypoxia chamber could be used to study whether or not the effect is caused by ligand secretion, as laminar flow would induce a specific spatial direction wherein cells start producing cAMP. Finally, experiments aiming to potentially confirm the involvement of specific ligands and receptors could be performed by blocking receptors, for example using propranolol to block β adrenergic receptors, or by inhibiting ligand synthesis, for example using nonsteroidal anti-inflammatory drugs (NSAIDs) to block prostaglandin synthesis[82]. All in all, further research into this effect using real-time fluorescence lifetime microscopy in combination with EPAC-based FLIM biosensors and the custom-build hypoxia chamber could potentially provide useful insights into the signaling involved in mediating hypoxic preconditioning.

Temperature project

This second project aimed to investigate whether and how temperature influences the cAMP pathway signaling kinetics, using the EPAC-S[H201] cAMP biosensor and STELLARIS 8 confocal scanning microscope with FLIM capabilities, equipped with a stage top incubator. Initial experiments indeed showed that EPAC-S[H201] biosensor lifetime increases in response to elevated temperature, and return to baseline in response to a subsequent decrease in temperature. To validate this lifetime increases is caused by cAMP, the same experiment was repeated on cells transfected with a biosensor variant that contains a mutated cAMP binding site, lowering its affinity for cAMP. This mutated sensor did not show the previously observed lifetime increase in response to elevated temperature, suggesting the effect was indeed caused by a cAMP-mediated conformational change. A variety of different experiments were performed next to further confirm that the binding of cAMP to the biosensor is required for increased lifetimes in response to elevated temperature, some of which remained inconclusive. Firstly, experiments attempting to block the temperature-mediated lifetime increase by pharmacologically inhibiting adenylyl cyclase were proven to be inconclusive, since the inhibitor did not sufficiently inhibit cAMP synthesis by adenylyl cyclase. Secondly, experiments utilizing two different ratiometric FRET sensors for PKA activity yielded inconsistent results, likely because focus drift due to thermal expansion masked any true change in FRET ratio. However, useful insights were obtained through the two following experiments. Submitting COS7 *GNAS* knockout cells to elevated temperatures revealed that the conventional signaling cascade to activate adenylyl cyclase through $G_{\alpha s}$ is not involved in the increased biosensor lifetimes in at elevated temperatures. This result instead suggest that adenylyl cyclase could be intrinsically heat-sensitive, or that we were observing heat-induced artifacts in the EPAC-S[H201] biosensor, such as unfolding or aggregation. An ELISA performed to detect cAMP in cell lysates finally showed that no elevated cAMP concentration is present in the lysate from cells that were exposed to heat, strongly supporting the hypothesis that the observed increased lifetimes were caused by a heat-induced artifact in biosensor conformation. Furthermore, overnight experiments showed the formation of biosensor-enriched bodies specifically in cells displaying long-term elevated lifetimes, potentially further reinforcing the hypothesis that biosensors had unfolded or aggregated. Finally, two distinct cell populations displaying different heat-induced lifetime responses were observed within the same experiment, suggesting a cellular stress response is actively involved in the suspected biosensor aggregation or denaturing. In conclusion, while this project has shown fluorescence lifetime imaging can be used to stably image biosensors during temperature shifts, the suspected heat-induced artifacts mean this specific FRET biosensor could not be used to reliably study cAMP dynamics in response to elevated temperatures.

Reliability of the mutated biosensor
After performing the ELISA and *GNAS* knockout experiments and thereby obtaining the results that convincingly exclude a role for cAMP in the observed heat-induced lifetime increase, the reliability of the result obtained using the biosensor with a mutation in the cAMP binding site was doubted. As the cAMP-binding site of EPAC-S[H201] is obviously involved in regulating the conformation of the biosensor, it is not unreasonable to hypothesize a mutation that changes the properties of the cAMP-binding site will affect this conformational change of the biosensor. This would possibly affect the hypothesized conformational changes due to heat-induced unfolding or aggregation of the biosensor, which could explain the different behavior displayed by the mutated sensor compared to EPAC-S[H201] under elevated temperatures.

Biosensor misfolding and subsequent aggregation
We hypothesize the observed lifetime increase of the EPAC-S[H201] biosensor at elevated temperatures is caused by heat-induced protein unfolding and possibly subsequent aggregation. Heat-induced unfolding has been proposed to occur in a FRET-based biosensor with a structure similar to that of the EPAC-S[H201] biosensor before, in which this misfolding is thought to increase the distance between the donor and acceptor fluorophores beyond the <10 nm required for efficient FRET[83]. This is in line with the long lifetimes (i.e. low FRET efficiency) we observe at elevated temperatures. It is also a possibility that this hypothesized biosensor unfolding is actively induced by heat-activated

chaperone proteins, commonly referred to as Heat-Shock Proteins (HSPs), which could potentially assist in folding the EPAC-S[H201] sensor to its low-FRET state at elevated temperatures, independently of cAMP[84].

There are observations in literature that could support the idea that the EPAC-S[H201] biosensor has the ability to aggregate. First of all, previous generations of EPAC-based cAMP FRET-sensors would occasionally form highly fluorescent aggregates, which is thought to be caused by aggregation of the fluorophores[11]. Furthermore, the EPAC protein contains a RA domain, a domain that known to be able to form dimers[85,86]. In EPAC, this domain is normally masked by the cAMP binding domain, but one can hypothesize this domain becomes exposed in a misfolded EPAC-based biosensor, where it could mediate formation of biosensor clusters[85].

A potentially powerful tool to study whether the EPAC-S[H201] biosensor aggregates *in vitro* is Fluorescence Correlation Spectroscopy (FCS). In FCS, the fluorescence emission in a very small solution volume (~1 μm^3) containing fluorescent particles is measured. Fluctuations in the measured fluorescence intensity, which can be attributed to Brownian motion of the fluorescent particles within the observation volume, can be used obtain quantitative data on fluorescent particle size and fluorescent particle concentration[87]. Using these two parameters, the hypothesized EPAC-S[H201] biosensor aggregation when exposed to elevated temperatures can be studied, as formation of aggregates would result in increased fluorescent particle size and decreased fluorescent particle concentration.

Stress bodies and aggregated biosensors

The hypothesis that the EPAC-S[H201] biosensor misfolds or aggregates at elevated temperatures could be further supported by the observed formation of biosensor-enriched stress bodies during overnight experiments in cells exposed to elevated temperatures. At present, we do not know exactly what the observed biosensor-enriched bodies are, however numerous different heat-activated cellular stress responses are known to be associated the formation of stress bodies[77,88,89]. One possibility is that these biosensor-enriched bodies are stress-induced autophagosomes, formed in an effort to degrade the hypothesized heat-induced biosensor aggregates[88]. On the other hand, it is possible that these stress bodies are not a cellular response against undesired protein aggregation, but rather a stress response in which proteins are actively aggregated. An example of such a mechanism are stress granules, reversible membrane-less compartments that are formed by active aggregation of RNA-binding proteins, and therefore consist mainly of mRNA, but also contain a diverse range of other aggregated proteins trapped within the stress granule[77,89–91].

Either of these two highlighted cases could potentially offer an explanation as to why low FRET efficiency (long lifetime) is observed in the biosensor-enriched bodies, instead of the high FRET efficiency (short lifetime) one would expect when biosensors are densely clustered together. In the hypothesis where EPAC-S[H201] biosensors spontaneously aggregate under elevated temperatures and are degraded by autophagosomes, it could be that these aggregates have an amyloid morphology. Amyloid aggregates are highly structured, with all monomers being oriented in the same direction[92]. For the hypothesized EPAC-S[H201] biosensor aggregates, it is possible that all donor fluorophores would be oriented on one side of the aggregate, while the acceptor fluorophores are oriented on the other side. Therefore, no FRET would be possible between them. In the case of the stress granules, biosensor monomers would likely be somewhat spatially separated due to the granule mostly consisting of mRNA molecules, limiting FRET between different EPAC-S[H201] monomers. In any case, further research would be required to draw conclusions about the nature of these biosensor-enriched stress bodies and their relation to possible biosensor misfolding or aggregation. Initial options to investigate the observed stress bodies include higher resolution imaging to obtain a clear view on size and morphology, as well as performing fixed immunostainings for biomarkers associated with specific stress-induced bodies, for example autophagosomes.

Materials & Methods

Cell culture

HeLa, MelJuSo and B16F10 cell lines stably expressing the EPAC-S^{H201} construct were established by J. Klarenbeek and O. Kukk. Monoclonal COS7 (clone 17) and subsequently derived monoclonal COS7 *GNAS* knockout (clone 2) cell lines stably expressing the EPAC-S^{H250} construct were established by S. Mukherjee and A. Loncq de Jong. Details on the EPAC-S^{H201} and EPAC-S^{H250} constructs can be found in Table 1. All cell lines were cultured in DMEM (Gibco) supplemented with 10% FCS (Gibco) and incubated in a humidified incubator at 37°C with 5% CO_2. Cells were grown to ~80% confluency and subsequently passaged every 2-3 days. For passaging, cells were washed with 4 mL PBS and detached with 2 mL 1x Trypsin-EDTA (Sigma-Aldrich). For imaging experiments, the desired amounts of cells were seeded on 24 mm coverslips (Thermo Scientific) in 6-well plates the day before performing the experiment. Coverslips were previously sterilized with 70% ethanol after which each coverslip was stored in individual wells in the 6-well plates.

Table 1. Details on stably expressed constructs used in this report.

Unique lab identifier	Details
H201	Q2-mT2Del_EPACdDEPCD_Q270E_tdBlackcp173Ven(ST)
H250	Q2-mT2Del-EPACdDEPCD_Q270E_tdBlcp173Ven(ST)-2A-pamCherry-HNS

Transient transfections

HeLa cells were seeded in 6-well plates containing 24 mm coverslips 24 hours prior to transient transfection, and transient transfection was performed 48 hours prior to performing an experiment. For each well, 1 µg plasmid DNA and 3 µL FuGENE (Promega) were mixed in 200 µL serum-free DMEM and incubated for 20-30 minutes, after which 200 µL of the mix was added to each well drop-by-drop. For co-transfections, 1 µg of each plasmid was mixed with 6 µL FuGENE in 200 µL serum-free DMEM instead. Further details on transiently transfected constructs used in this report can be found in Table 2.

Table 2. Details on transiently transfected constructs used in this report.

Unique lab identifier	Details
C124	mTurq2-C2
C136	tdblcpV-hinge
H1	Cat-YFP
H2	RII-CFP
H86	AKAR2
H249	mT2Del-EpacDDEP-C.D.(R279L)-ttdblcp173Ven(ST)

Reagents

Isoproterenol, propranolol, forskolin, 3-isobutyl-1-methylxanthine (IBMX) and α-melanocyte-stimulating hormone (α-MSH) were purchased from Sigma-Aldrich. Cobalt chloride ($CoCl_2$) (Sigma-Aldrich) was kindly provided by the Medema lab. Different 2',5'-Dideoxyadenosine (ddA) batches were purchased from Sigma-Aldrich and ChemCruz. 4,5-dimethoxy-2-nitrobenzyl 3',5'-cyclic adenosine monophosphate (DMNB-caged cAMP) was synthesized by collaborators from the Max Planck Institute of Molecular Cell Biology and Genetics in Dresden, Germany. The source of prostaglandin E_1 (PGE1) is unknown.

Microscopes

Three different microscopes were used in this report: Leica STELLARIS 8 FALCON (FAst Lifetime CONtrast), Leica SP8 FALCON, and Leica DMIRE2 equipped with a Lamber Instruments FLIM Attachment (LIFA) for FD-FLIM.

Leica STELLARIS 8 FALCON

Experiments on the Leica STELLARIS 8 FALCON were carried out using Leica LAS-X software version 4.3. FLIM experiments were performed using a HC PL APO CS2 20x/0.75 dry objective with the pinhole set to 3.0 AU, except for the drug titration experiments on B16F10 cells, which was performed using a HC PL APO CS2 40x/1.10 water objective with the pinhole set to 3.0 AU. The EPAC-S biosensor donor fluorophore (mTurquoise2) was excited using the 440 nm line of the White Light Laser (WLL). Donor fluorophore photon arrival times were recorded using a Power HyD detector set to count photons between 450 and 510 nm. Timelapses were taken using a frame interval of 5 seconds, except for overnight experiments, which were taken at frame intervals of either 30 or 60 seconds. For all experiments, the focal plane was stabilized using the Leica Adaptive Focus Control (AFC), which was set to refocus every frame of the timelapse. For ratio-based FRET quantification experiments, the HC PL APO CS2 20x/0.75 dry objective was used with the pinhole set to 3.0 AU. Donor fluorophores were excited using the 440 nm WLL line, and photon emission was detected using two Power HyD detectors set to 450-510 nm and 520-600 nm for the CFP donor and YFP acceptor fluorophores, respectively. The remaining settings were the same as described for FLIM experiments.

Leica SP8 FALCON

Experiments on the Leica SP8 FALCON were performed using Leica LAS-X software version 3.5. FLIM experiments were carried out using a HC PL APO CS2 20x/0.75 dry objective, and the pinhole was set to 3.0 AU. Cells were excited using a pulsed diode laser (PicoQuant) at 440 nm. Photon arrival times were recorded using a hybrid detector, recording photons between 450 and 510 nm. Timelapses were taken with 5 second frame intervals, and AFC was used to stabilize the focal plane. The same setup was used for ratio-based FRET efficiency quantification experiments, except two hybrid detectors were used to measure emission intensity between 450-510 nm and 520-600 nm for donor and acceptor fluorophore emission, respectively.

LIFA FD-FLIM

The Leica DMIRE2 is equipped with a LIFA camera built by Lamberts Instruments, and runs on accompanying LIFA software by Lamberts Instruments. Rhodamine 6G was used as a lifetime reference dye (τ = 3.93 ns at 37°C). Cells were imaged using a HCX PL APO 40x/1.25 PH 3 CS oil objective. mTurquoise2 donor fluorophores were excited using a 445 nm LED at a modulation frequency of 40 MHz and an exposure time of 100 ms, recorded with 12 phase steps. A frame interval of 10 seconds was used for the timelapses.

Data processing

Leica STELLARIS 8 FALCON and Leica SP8 FALCON

Pixel photon arrival times from experiments with EPAC-based cAMP FRET sensors typically show a multi-exponential decay curve, because the individual biosensors within that pixel can be in different FRET states. The multi-exponential decay curve observed during our FLIM experiments is best described by a double-exponential reconvolution model, using a fixed lifetime of 0.9 ns for the high FRET state and 3.9 ns for the low FRET state. These fixed lifetime values are characteristic for EPAC-S[H201] biosensor and were obtained from a polar plot created within Leica LAS-X software based on experimental FLIM data (Figure S3). In the LAS-X software, pixel photon arrival times were binned (2x2 pixels) and fitted to the double-exponential reconvolution model using the fixed lifetimes of 0.9 and 3.9 ns. This creates two intensity images, which contain the amplitudes of the short or long lifetime components, respectively. These 2-component fitted images were exported as TIF files for fast and convenient processing using Fiji[93]. In Fiji, intensity-weighted lifetimes for are calculated from the 2-component fitted images by multiplying the short and long lifetime intensity components by their respective fixed lifetime value, after which the sum of these two multiplications is divided by the sum of the intensities in the original image, as summarized in the following formula:

$$\tau = \frac{0.9 \times \text{Int1} + 3.9 \times \text{Int2}}{\text{Int1} + \text{Int2}}$$

Two different Fiji macros written by B. van den Broek were used to calculate these weighted lifetimes, and to display the calculated lifetimes in graphs. In the first macro (FALCON_get_lifetime_from_2fit_OK.ijm) the average weighted lifetime of the entire field of view is calculated for each frame in the timelapse and displayed in a graph as a lifetime trace over time. In the second macro (Analyze_FLIM_timelapse_experiments_1.6.ijm) cells are first segmented using a deep-learning based cell segmentation algorithm called Cellpose, after which the average weighted lifetime for each segmented cell is calculated for every frame in the timelapse[68]. The resulting lifetime images are then visualized as a movie overlaid on accompanying intensity images, as well as in a graph displaying cell-specific lifetime traces over time and in a kymograph-like image sorted on cellular response.

LIFA FD-FLIM

Data obtained using the LIFA FD-FLIM microscope system is exported as a Lamberts Instruments file format (.fli) by the LIFA software for further processing and analysis using Fiji. In Fiji, lifetimes are calculated from the raw exported data and the accompanying Rhodamine 6G reference lifetime file using a Fiji plugin (Frequency_FLIM_analysis-1.01.jar) written by R. Harkes. This plugin was integrated into the above-mentioned cell segmentation-based lifetime analysis macro by B. van den Broek. Therefore, data is again ultimately processed into a timelapse of calculated lifetime images overlaid onto accompanying intensity images, and graphs plotting the lifetime traces of individual cells over time.

Measuring molecular oxygen concentration

Molecular oxygen concentrations were measured using a FireStingO2 fiber-optical oxygen meter (FSO2-2, PyroScience) featuring two optical channels, running on PC-controlled Pyro Oxygen Logger software (Firmware 3.7, Version 3.317, PyroScience). The FireStingO2 uses OXSP5 oxygen sensor spots (PyroScience) to measure oxygen concentrations. These sensor sports contain dyes that are excited by red light and show oxygen-dependent luminescence in the near-infrared spectrum. Excitation and luminescence light travels from and to the FireStingO2 through optical fibers. Atmospheric oxygen concentrations within the hypoxia chamber were measured by an OXSP5 glued to the tip of an inwards-pointing hollow screw, that is screwed into the hypoxia chamber wall. An optical fiber from outside the hypoxia chamber was inserted into the hollow screw, making contact with the OXSP5. This channel for measuring atmospheric oxygen was calibrated by 21% oxygen and 0% oxygen measurements, obtained in ambient air and in a plastic bag inflated with pure nitrogen gas, respectively. Dissolved oxygen concentrations within the hypoxia chamber were measured by adhering an OXSP5 to the inside-facing side of a glass coverslip in the hypoxia chamber, and stabilizing an optical fiber underneath the OXSP5 on the outside of the hypoxia chamber, measuring through the glass coverslip. This was not compatible with live-cell imaging experiments, since there would be cells attached to the coverslip and the optic fiber would be blocked from reaching the OXSP5 by the objective. The optical channel used to measure dissolved oxygen concentration was calibrated using 100% and 0% oxygen-saturated tap water, obtained by bubbling with air and with pure nitrogen gas, respectively.

Gas mixing system

The gas mixing system used during this project is custom-build by our lab. It consists of three EL-FLOW (Bronkhorst High-Tech) gas mass flow meters and controllers, with one being attached to pure nitrogen, air and pure carbon dioxide gas supply systems each. The mass flow meters were powered by two digital readout control systems (E-5752 series, Bronkhorst High-Tech), which allowed for control over the contents of the gas mixture. Used gas mixes consisted of either air or nitrogen, depending on whether desired conditions were normoxic or hypoxic, supplemented by carbon dioxide for use with bicarbonate-buffered solutions. The required amount of carbon dioxide for the desired pH of 7.3 was determined by bubbling bicarbonate-buffered medium containing phenol red with a gas mixture that was supplemented with carbon dioxide, and visually assessing at which fraction carbon dioxide the desired pH was

reached. This was further confirmed using a portable pH meter (Testo 206-pH1). The final gas mixture was split between two outlet tube lines, one of which was used to flow the gas mixture into the hypoxia chamber, while the other was used for bubbling medium and buffers.

Increasing drug concentration titrations

All drug dilutions were made in separate 50 mL polypropylene tubes (Sarstedt) containing 10 ml HEPES-CBS-Glucose buffer (HCG; 140 mM NaCl, 5 mM KCl, 1 mM $MgCl_2$, 1 mM $CaCl_2$, 23 mM $NaHCO_3$, 10 mM HEPES, 10 mM glucose, pH 7.3). The drug dilutions were always first used for an experiment under normoxic conditions, after which those same drug dilutions were nitrogen bubbled for an experiment under hypoxic conditions. If required for a reoxygenated control experiment, those same drug dilutions were subsequently reoxygenated by air bubbling. In between these experiments, the syringes and tubing of the hypoxia chamber fluid control system were thoroughly cleaned by flushing with Milli-Q, followed by 70% ethanol, another round of Milli-Q and finally HCG buffer (deoxygenated, if required). Prior to performing hypoxia experiments, 10 mL HCG buffer was deoxygenated by nitrogen bubbling for 5 minutes. 1 mL deoxygenated HCG buffer was pipetted onto the coverslip with cells before quickly closing the hypoxia chamber and activating hypoxic gas flow. An additional 3 mL deoxygenated HCG buffer was added into the hypoxia chamber through the fluid inlet syringe. The chamber was incubated in this manner for 15-20 minutes until the atmospheric and dissolved oxygen was at a minimum. During this incubation time, the 5 tubes containing the drug dilution were each nitrogen bubbled for 3 minutes and immediately closed off after. Each tube would be bubbled for an additional 2 minutes during the experiment, right before being injected into the hypoxia chamber. After starting the timelapse, a 100 second lifetime baseline was measured, after which 2.5 mL HCG buffer was removed from the hypoxia chamber through the outlet syringe and immediately replaced by 2.5 mL deoxygenated drug dilution through the inlet syringe. The dead volume of the fluid outlet and inlet tubing was 0.5 mL each, meaning effectively 2 mL HCG buffer was replaced by 2 mL fresh deoxygenated drug dilution. This process was repeated every 200 seconds until all 5 drug dilutions had been used. Finally, a non-deoxygenated forskolin dilution was used as a positive control. The experimental protocol for normoxia and reoxygenated experiments was exactly the same, except drug dilutions were never nitrogen bubbled prior to normoxia experiments, and bubbled with air instead of nitrogen prior to reoxygenated controls.

Isoproterenol-propranolol assay

Drug dilutions were made in 50 mL polypropylene tubes containing 10 mL FluoroBrite DMEM (Gibco). The drug dilutions were always first used for an experiment under normoxic conditions, after which those same drug dilutions were nitrogen bubbled for an experiment under hypoxic conditions. In between these experiments, the syringes and tubing of the hypoxia chamber fluid control system were thoroughly cleaned by flushing with Milli-Q, followed by 70% ethanol, another round of Milli-Q and finally FluoroBrite DMEM (deoxygenated, if required). For isoproterenol-propranolol assays, the fluid outlet tube was replaced by a second fluid inlet tube, in order to be able to sequentially add isoproterenol and propranolol within seconds. Prior to performing hypoxic experiments, 10 mL FluoroBrite DMEM was deoxygenated by nitrogen bubbling for 5 minutes. 1 mL deoxygenated FluoroBrite DMEM was quickly pipetted onto the coverslip with cells before quickly closing the hypoxia chamber and activating hypoxic gas flow. The hypoxia chamber was incubated in this manner for 10 minutes. During this time, isoproterenol and propranolol dilutions were both nitrogen bubbled for 5 minutes. After recording a baseline, 1 mL deoxygenated isoproterenol was injected into the hypoxia chamber, followed by 2 mL deoxygenated propranolol once the biosensor was reaching saturation. The experimental protocol for normoxic conditions was exactly the same, except drug dilutions were never nitrogen bubbled.

DMNB-cAMP uncaging in the hypoxia chamber

An Explorer One 355-1 (Spectra-Physics) 355 nm UV laser was used for the photo-release of DMNB-caged cAMP. In order to do so, the shutter on the Leica DMIRE2 was opened for about 1 second each round of uncaging. Prior to an experiment, cells were covered by 0.5 mL FluoroBrite DMEM containing 100 µM DMNB-caged cAMP and were

incubated in the hypoxia chamber for 30 minutes under normoxic conditions. A number of uncaging rounds in normoxia were performed first, after which the gas flow was switched to hypoxic conditions. After about 15 minutes of passive deoxygenation by hypoxic gas flow, repeated uncaging rounds in hypoxia were performed. Finally, the sample was reoxygenated by normoxic gas flow and a number of uncaging rounds were performed in normoxic conditions.

Western blot

Cells covered by 2 mL HCG buffer were incubated in the hypoxia chamber under the indicated conditions. For one sample condition, cells were incubated with 150 µM CoCl$_2$ 6 hours prior to the experiment. After completing the experiment, HCG buffer covering the cells was removed through the fluid outlet syringe, after which the hypoxia chamber was opened up. The coverslip was subsequently quickly removed from the Leiden coverslip holder and placed in a 6 well-plate, where cells were lysed in 50 µL 1x Laemmli buffer containing β-mercaptoethanol, kindly provided by the Medema lab. The lysis process was aided by scraping using a cell scraper. The lysate was transferred to an Eppendorf tube and heated to 95°C for 10 minutes, after which an insulin syringe was used to shear genomic DNA in the lysate. 30 µL from each lysate, along with 5 µL protein ladder (Fermentas PageRuler Prestained Protein Ladder), was separated by SDS-PAGE in a precast polyacrylamide gel (Invitrogen Bolt 4-12% Bis Tris Plus) and transferred to a nitrocellulose membrane. Membranes were blocked with bovine serum albumin in TBS for 60 minutes at 4°C, after which rabbit anti-HIF1α (Cayman Chemicals, 1/1000), kindly provided by the Medema lab, and mouse anti-alpha-tubulin (Sigma-Aldrich, 1/1000) antibodies were added to the blocking buffer and incubated overnight at 4°C. Membranes were washed with TBS-T three times for 10 minutes and incubated with HRP-conjugated secondary antibodies, kindly provided by the Rowland group, for 1 hour at 4°C. Membranes were again washed with TBS-T three times for 10 minutes. Proteins were visualized by chemiluminescence using Amersham ECL Western Blotting Detection Reagents (GE Healthcare) and a ChemiDoc (BioRad) imaging system.

Pimonidazole immunofluorescence

Cells covered by 2 mL HCG buffer containing 10 µM pimonidazole (Hypoxyprobe), kindly provided by the Medema lab, were incubated in the hypoxia chamber under either normoxic or hypoxic conditions for 1 hour. After completing this experiment, HCG buffer covering the cells was removed through the fluid outlet syringe, after which the hypoxia chamber was opened up. The coverslip was subsequently quickly removed from the Leiden coverslip holder and placed in a 6 well-plate where cells were fixed using 4% paraformaldehyde in PBS for 20 minutes at room temperature, permeabilized with Triton X-100 for 5 minutes at room temperature, washed with PBS and blocked with bovine serum albumin in PBS for 1 hour at room temperature. The samples were incubated with mouse anti-pimonidazole antibodies (Hypoxyprobe, 1/100), kindly provided by the Medema lab, for 1 hour at room temperature, followed by incubation with anti-mouse AlexaFluor 647 (Invitrogen, 1/1000) secondary antibodies for 1 hour at room temperature. Immunostained coverslips were mounted on microscope slides using Mowiol mounting medium and imaged using the Leica STELLARIS 8 FALCON with a HC PL APO CS2 20x/0.75 dry objective.

Temperature regulation during experiments
Leica STELLARIS 8 FALCON

The Leica STELLARIS 8 FALCON is equipped with a Bold Line Stage Top Incubator (OKO Lab). This stage top incubator has both a heated incubator body and a heated slidable glass cover, which allows for fast, accurate and uniform temperature changes, and is equipped with an accurate sample temperature sensor. This is all controlled through the accompanying OKO-TOUCH touch screen user interface. Prior to an experiment, a coverslip with cells was inserted into a pre-heated Leiden coverslip holder and 2 mL 37°C pre-heated FluoroBrite DMEM was added to the coverslip holder. The coverslip holder was then incubated in the microscope stage top incubator and the temperature sensor was inserted into the sample. Imaging timelapses were started after a short waiting period until the sample temperature had stabilized at 37°C. A typical experiment started with a 5 minute 37°C lifetime baseline, after which the temperature in the stage top incubator was elevated (often to 43°C) for 20 minutes using the OKO-TOUCH. The

full temperature change from 37°C to 43°C usually occurred within 10 minutes. Finally, in most experiments the temperature was reduced down to 30°C, which took around 15-20 minutes. The majority of elevated temperature experiments were performed on this system.

Leica SP8 FALCON
Since the Leica SP8 FALCON is not outfitted with a stage top incubator, but rather a microscope enclosure cage incubator (also manufactured by OKO Lab) that does not allow for efficient temperature changes, an alternative method to regulate temperature was developed. To this end, a Carl Zeiss TempControl 37 analog temperature regulated stage was attached to the Leica SP8 FALCON. Unlike the Leica STELLARIS 8 FALCON stage top incubator in which the temperature of the entire environment enclosed in the incubator is regulated, here only the temperature of the stage itself is regulated, causing the sample to be cooled by the surrounding environment. Therefore, for the sample to reach the desired temperatures, this stage had to be heated to higher temperatures. To make sure we could still accurately monitor the temperature of the sample itself, an OKO Lab sample temperature sensor of the same design as the one on the Leica STELLARIS 8 FALCON was used. Further experimental protocols are the same as described for experiments on the Leica STELLARIS 8 FALCON.

Enzyme-linked immunoassay
Cells were heated to the different indicated temperatures using the stage top incubator on the Leica STELLARIS 8 FALCON. A positive control sample was treated with 100 µM IBMX and 250 µM forskolin. Immediately after stopping the imaging timelapses, Leiden coverslip holders were placed directly on ice and cells were lysed according to the manufacturers protocol (Cyclic AMP XP Assay Kit #4339, Cell Signaling Technologies). Two background controls in which sample was substituted for either lysis buffer or Milli-Q were included. Technical duplicates were included in the assay. In order to determine the unknown cAMP concentrations in the ELISA reaction volumes, a standard curve using known cAMP concentrations (0.111, 0.333, 1, 3, 9, 27, 81, 243 nM cAMP) was included in the assay. The ELISA assay was performed according to the manufacturers protocol. Absorbance was measured using an Agilent BioTek Epoch spectrophotometer, and triplicate absorbance measurements were performed. During data processing, triplicate absorbance measurement values were averaged first, followed by averaging of the technical duplicate samples. A trendline (R^2 = 0.98) was created in Microsoft Excel based on the known cAMP concentrations. Unknown cAMP concentrations in the ELISA reaction volume were extrapolated from this trendline.

Acknowledgements

References

1. Sassone-Corsi, P. The cyclic AMP pathway. *Cold Spring Harb Perspect Biol* 4, a011148 (2012).

2. Daniel, P. B., Walker, W. H. & Habener, J. F. Cyclic AMP signaling and gene regulation. *Annu Rev Nutr* 18, 353–383 (1998).

3. Zhang, H., Kong, Q., Wang, J., Jiang, Y. & Hua, H. Complex roles of cAMP–PKA–CREB signaling in cancer. *Experimental Hematology & Oncology* 9, 1–13 (2020).

4. Harkes, R. *et al.* Dynamic FRET-FLIM based screening of signal transduction pathways. *Scientific Reports* 11, 1–13 (2021).

5. Bjarnadóttir, T. K. *et al.* Comprehensive repertoire and phylogenetic analysis of the G protein-coupled receptors in human and mouse. *Genomics* 88, 263–273 (2006).

6. de Rooij, J. *et al.* Epac is a Rap1 guanine-nucleotide-exchange factor directly activated by cyclic AMP. *Nature* 396, 474–477 (1998).

7. Nikolaev, V. O., Bünemann, M., Hein, L., Hannawacker, A. & Lohse, M. J. Novel Single Chain cAMP Sensors for Receptor-induced Signal Propagation. *Journal of Biological Chemistry* 279, 37215–37218 (2004).

8. DiPilato, L. M., Cheng, X. & Zhang, J. Fluorescent indicators of cAMP and Epac activation reveal differential dynamics of cAMP signaling within discrete subcellular compartments. *Proceedings of the National Academy of Sciences* 101, 16513–16518 (2004).

9. Ponsioen, B. *et al.* Detecting cAMP-induced Epac activation by fluorescence resonance energy transfer: Epac as a novel cAMP indicator. *EMBO Rep* 5, 1176–1180 (2004).

10. Klarenbeek, J. B., Goedhart, J., Hink, M. A., Gadella, T. W. J. & Jalink, K. A mTurquoise-based cAMP sensor for both FLIM and ratiometric read-out has improved dynamic range. *PLoS One* 6, e19170 (2011).

11. Klarenbeek, J., Goedhart, J., van Batenburg, A., Groenewald, D. & Jalink, K. Fourth-generation epac-based FRET sensors for cAMP feature exceptional brightness, photostability and dynamic range: characterization of dedicated sensors for FLIM, for ratiometry and with high affinity. *PLoS One* 10, e0122513 (2015).

12. Jares-Erijman, E. A. & Jovin, T. M. FRET imaging. *Nat Biotechnol* 21, 1387–1395 (2003).

13. Bajar, B. T., Wang, E. S., Zhang, S., Lin, M. Z. & Chu, J. A guide to fluorescent protein FRET pairs. *Sensors* 16, 1488 (2016).

14. Sekar, R. B. & Periasamy, A. Fluorescence resonance energy transfer (FRET) microscopy imaging of live cell protein localizations. *J Cell Biol* 160, 629–633 (2003).

15. Periasamy, A., Mazumder, N., Sun, Y., Christopher, K. G. & Day, R. N. FRET microscopy: basics, issues and advantages of FLIM-FRET imaging. in *Advanced Time-Correlated Single Photon Counting Applications* 249–276 (Springer, 2015).

16. Leavesley, S. J. & Rich, T. C. Overcoming limitations of FRET measurements. *Cytometry. Part A: the journal of the International Society for Analytical Cytology* 89, 325 (2016).

17. Datta, R., Heaster, T. M., Sharick, J. T., Gillette, A. A. & Skala, M. C. Fluorescence lifetime imaging microscopy: fundamentals and advances in instrumentation, analysis, and applications. *J Biomed Opt* 25, 71203 (2020).

18. Becker, W. Fluorescence lifetime imaging–techniques and applications. *J Microsc* 247, 119–136 (2012).

19. de Los Santos, C., Chang, C., Mycek, M. & Cardullo, R. A. FRAP, FLIM, and FRET: Detection and analysis of cellular dynamics on a molecular scale using fluorescence microscopy. *Mol Reprod Dev* 82, 587–604 (2015).

20. Alvarez, L. A. J. *et al.* SP8 FALCON: A novel concept in fluorescence lifetime imaging enabling video-rate confocal FLIM. *Nat. Methods* 16, 1069–1071 (2019).

21. Padilla-Parra, S., Audugé, N., Coppey-Moisan, M. & Tramier, M. Quantitative FRET analysis by fast acquisition time domain FLIM at high spatial resolution in living cells. *Biophys J* 95, 2976–2988 (2008).

22. Raspe, M. *et al.* siFLIM: single-image frequency-domain FLIM provides fast and photon-efficient lifetime data. *nature methods* 13, 501–504 (2016).

23. Levitt, J. A. *et al.* Quantitative real-time imaging of intracellular FRET biosensor dynamics using rapid multi-beam confocal FLIM. *Sci Rep* 10, 1–9 (2020).

24. Goedhart, J. *et al.* Structure-guided evolution of cyan fluorescent proteins towards a quantum yield of 93%. *Nat Commun* 3, 1–9 (2012).

25. Lee, P., Chandel, N. S. & Simon, M. C. Cellular adaptation to hypoxia through hypoxia inducible factors and beyond. *Nature reviews Molecular cell biology* 21, 268–283 (2020).

26. Carreau, A., Hafny-Rahbi, B. el, Matejuk, A., Grillon, C. & Kieda, C. Why is the partial oxygen pressure of human tissues a crucial parameter? Small molecules and hypoxia. *J Cell Mol Med* 15, 1239–1253 (2011).

27. McKeown, S. R. Defining normoxia, physoxia and hypoxia in tumours—implications for treatment response. *Br J Radiol* 87, 20130676 (2014).

28. Ivan, M. *et al.* HIFα targeted for VHL-mediated destruction by proline hydroxylation: implications for O2 sensing. *Science (1979)* 292, 464–468 (2001).

29. Jaakkola, P. *et al.* Targeting of HIF-α to the von Hippel-Lindau ubiquitylation complex by O2-regulated prolyl hydroxylation. *Science (1979)* 292, 468–472 (2001).

30. Harris, A. L. Hypoxia—a key regulatory factor in tumour growth. *Nature reviews cancer* 2, 38–47 (2002).

31. Dong, Z. *et al.* Up-regulation of apoptosis inhibitory protein IAP-2 by hypoxia: HIF-1-independent mechanisms. *Journal of Biological Chemistry* 276, 18702–18709 (2001).

32. Lee, S.-H., Golinska, M. & Griffiths, J. R. HIF-1-Independent Mechanisms Regulating Metabolic Adaptation in Hypoxic Cancer Cells. *Cells* 10, 2371 (2021).

33. Erler, J. T. *et al.* Hypoxia-mediated down-regulation of Bid and Bax in tumors occurs via hypoxia-inducible factor 1-dependent and-independent mechanisms and contributes to drug resistance. *Mol Cell Biol* 24, 2875–2889 (2004).

34. Simko, V. *et al.* Hypoxia induces cancer-associated cAMP/PKA signalling through HIF-mediated transcriptional control of adenylyl cyclases VI and VII. *Sci Rep* 7, 1–11 (2017).

35. Shaikh, D. *et al.* cAMP-dependent protein kinase is essential for hypoxia-mediated epithelial–mesenchymal transition, migration, and invasion in lung cancer cells. *Cell Signal* 24, 2396–2406 (2012).

36. Millen, J., MacLean, M. R. & Houslay, M. D. Hypoxia-induced remodelling of PDE4 isoform expression and cAMP handling in human pulmonary artery smooth muscle cells. *Eur J Cell Biol* 85, 679–691 (2006).

37. Baloglu, E., Ke, A., Abu-Taha, I. H., Bartsch, P. & Mairbaurl, H. In vitro hypoxia impairs β2-adrenergic receptor signaling in primary rat alveolar epithelial cells. *American Journal of Physiology-Lung Cellular and Molecular Physiology* 296, L500–L509 (2009).

38. Cheong, H. I. *et al.* Hypoxia sensing through β-adrenergic receptors. *JCI Insight* 1, (2016).

39. Sun, Y. *et al.* beta-blocker reverses inhibition of beta-2 adrenergic receptor resensitization by hypoxia. *bioRxiv* 2020.09.17.301903 (2020) doi:10.1101/2020.09.17.301903.

40. Schmedtje Jr, J. F., Liu, W.-L. & Chen, Y. pH is critical to the regulation of expression of the β2-adrenergic receptor gene in hypoxia. *Biochimica et Biophysica Acta (BBA)-Molecular Cell Research* 1314, 25–33 (1996).

41. Lombardi, M. S. *et al.* Hypoxia/ischemia modulates G protein–coupled receptor kinase 2 and β-arrestin-1 levels in the neonatal rat brain. *Stroke* 35, 981–986 (2004).

42. Mou, L. & Jackson, D. A. Transient hypoxia differentially decreases GRK2 protein levels in CHO cells stably expressing the m1 mAChR. *Biochemical and Biophysical Research Communications* 286, 848–851 (2001).

43. Lappano, R. *et al.* Recent advances on the role of G protein-coupled receptors in hypoxia-mediated signaling. *AAPS J* 18, 305–310 (2016).

44. Sodhi, A. *et al.* The Kaposi's sarcoma-associated herpes virus G protein-coupled receptor up-regulates vascular endothelial growth factor expression and secretion through mitogen-activated protein kinase and p38 pathways acting on hypoxia-inducible factor 1α. *Cancer Res* 60, 4873–4880 (2000).

45. Buscà, R. *et al.* Hypoxia-inducible factor 1α is a new target of microphthalmia-associated transcription factor (MITF) in melanoma cells. *J Cell Biol* 170, 49–59 (2005).

46. Varga, B. *et al.* Protective effect of alpha-melanocyte-stimulating hormone (α-MSH) on the recovery of ischemia/reperfusion (I/R)-induced retinal damage in a rat model. *Journal of Molecular Neuroscience* 50, 558–570 (2013).

47. Abramovitch, R. *et al.* A pivotal role of cyclic AMP-responsive element binding protein in tumor progression. *Cancer Res* 64, 1338–1346 (2004).

48. Taylor, C. T., Furuta, G. T., Synnestvedt, K. & Colgan, S. P. Phosphorylation-dependent targeting of cAMP response element binding protein to the ubiquitin/proteasome pathway in hypoxia. *Proceedings of the National Academy of Sciences* 97, 12091–12096 (2000).

49. Wenger, R. H., Kurtcuoglu, V., Scholz, C. C., Marti, H. H. & Hoogewijs, D. Frequently asked questions in hypoxia research. *Hypoxia* 3, 35 (2015).

50. Caterina, M. J. *et al.* The capsaicin receptor: a heat-activated ion channel in the pain pathway. *Nature* 389, 816–824 (1997).

51. McKemy, D. D., Neuhausser, W. M. & Julius, D. Identification of a cold receptor reveals a general role for TRP channels in thermosensation. *Nature* 416, 52–58 (2002).

52. Salzer, I., Ray, S., Schicker, K. & Boehm, S. Nociceptor signalling through ion channel regulation via GPCRs. *Int J Mol Sci* 20, 2488 (2019).

53. Lee, H. & Caterina, M. J. TRPV channels as thermosensory receptors in epithelial cells. *Pflügers Archiv* 451, 160–167 (2005).

54. Gouin, O. *et al.* TRPV1 and TRPA1 in cutaneous neurogenic and chronic inflammation: pro-inflammatory response induced by their activation and their sensitization. *Protein Cell* 8, 644–661 (2017).

55. Faro, D., Boekhoff, I., Gudermann, T. & Breit, A. Physiological temperature changes fine-tune β2-adrenergic receptor-induced cytosolic cAMP accumulation. *Molecular Pharmacology* 100, 203–216 (2021).

56. Lerro, K. A., Orlando, R., Zhang, H. Z., Usherwood, P. N. R. & Nakanishi, K. Separation of the sticky peptides from membrane proteins by high-performance liquid chromatography in a normal-phase system. *Anal Biochem* 215, 38–44 (1993).

57. Sereda, T. J., Mant, C. T., Sönnichsen, F. D. & Hodges, R. S. Reversed-phase chromatography of synthetic amphipathic α-helical peptides as a model for ligand/receptor interactions Effect of changing hydrophobic environment on the relative hydrophilicity/hydrophobicity of amino acid side-chains. *Journal of Chromatography A* 676, 139–153 (1994).

58. Ghanouni, P. *et al.* The effect of pH on β2 adrenoceptor function: Evidence for protonation-dependent activation. *Journal of Biological Chemistry* 275, 3121–3127 (2000).

59. Modest, V. E. & Butterworth IV, J. F. Effect of pH and lidocaine on β-adrenergic receptor binding: interaction during resuscitation? *Chest* 108, 1373–1379 (1995).

60. Pérez Piñero, C., Bruzzone, A., Sarappa, M. G., Castillo, L. F. & Lüthy, I. A. Involvement of α2-and β2-adrenoceptors on breast cancer cell proliferation and tumour growth regulation. *Br J Pharmacol* 166, 721–736 (2012).

61. Hao, G., Xu, Z. P. & Li, L. Manipulating extracellular tumour pH: an effective target for cancer therapy. *RSC Adv* 8, 22182–22192 (2018).

62. Chen, M. *et al.* Extracellular pH is a biomarker enabling detection of breast cancer and liver cancer using CEST MRI. *Oncotarget* 8, 45759 (2017).

63. Lee, S.-H. & Griffiths, J. R. How and why are cancers acidic? Carbonic anhydrase IX and the homeostatic control of tumour extracellular pH. *Cancers (Basel)* 12, 1616 (2020).

64. Görner, H. Effects of 4, 5-dimethoxy groups on the time-resolved photoconversion of 2-nitrobenzyl alcohols and 2-nitrobenzaldehyde into nitroso derivatives. *Photochemical & Photobiological Sciences* 4, 822–828 (2005).

65. Kohl-Landgraf, J. *et al.* Mechanism of the photoinduced uncaging reaction of puromycin protected by a 6-nitroveratryloxycarbonyl group. *J Am Chem Soc* 136, 3430–3438 (2014).

66. Stokfisz, K., Ledakowicz-Polak, A., Zagorski, M. & Zielinska, M. Ischaemic preconditioning–Current knowledge and potential future applications after 30 years of experience. *Adv Med Sci* 62, 307–316 (2017).

67. Heusch, G. Molecular basis of cardioprotection: signal transduction in ischemic pre-, post-, and remote conditioning. *Circ Res* 116, 674–699 (2015).

68. Stringer, C., Wang, T., Michaelos, M. & Pachitariu, M. Cellpose: a generalist algorithm for cellular segmentation. *Nature Methods* 18, 100–106 (2021).

69. Masaki, Y. *et al.* Imaging mass spectrometry revealed the accumulation characteristics of the 2-nitroimidazole-based agent "pimonidazole" in hypoxia. *PLoS One* 11, e0161639 (2016).

70. Menegakis, A. *et al.* Resistance of Hypoxic Cells to Ionizing Radiation Is Mediated in Part via Hypoxia-Induced Quiescence. *Cells* 10, 610 (2021).

71. Berezin, M. Y. & Achilefu, S. Fluorescence lifetime measurements and biological imaging. *Chem Rev* 110, 2641–2684 (2010).

72. Désaubry, L., Shoshani, I. & Johnson, R. A. 2′, 5′-Dideoxyadenosine 3′-polyphosphates are potent inhibitors of adenylyl cyclases. *Journal of Biological Chemistry* 271, 2380–2382 (1996).

73. Zhang, J., Ma, Y., Taylor, S. S. & Tsien, R. Y. Genetically encoded reporters of protein kinase A activity reveal impact of substrate tethering. *Proceedings of the National Academy of Sciences* 98, 14997–15002 (2001).

74. Zhang, J., Hupfeld, C. J., Taylor, S. S., Olefsky, J. M. & Tsien, R. Y. Insulin disrupts β-adrenergic signalling to protein kinase A in adipocytes. *Nature* 437, 569–573 (2005).

75. Omura, M., Grosmaitre, X., Ma, M. & Mombaerts, P. The β2-adrenergic receptor as a surrogate odorant receptor in mouse olfactory sensory neurons. *Molecular and Cellular Neuroscience* 58, 1–10 (2014).

76. Liu, H., Wenzel-Seifert, K. & Seifert, R. The olfactory G protein Gαolf possesses a lower GDP-affinity and deactivates more rapidly than Gsαshort: consequences for receptor-coupling and adenylyl cyclase activation. *J Neurochem* 78, 325–338 (2001).

77. Palangi, F., Samuel, S. M., Thompson, I. R., Triggle, C. R. & Emara, M. M. Effects of oxidative and thermal stresses on stress granule formation in human induced pluripotent stem cells. *PLoS One* 12, e0182059 (2017).

78. Goebel-Stengel, M., Stengel, A., Taché, Y. & Reeve Jr, J. R. The importance of using the optimal plasticware and glassware in studies involving peptides. *Anal Biochem* 414, 38–46 (2011).

79. Bratcher, P. E. & Gaggar, A. Characterization and prevention of the adsorption of surfactant protein D to polypropylene. *PLoS One* 8, e73467 (2013).

80. Fischer, M. J. E., van Oosterhout, A. J. M., Janssen, L. H. M. & Nijkamp, F. P. Effect of albumin on adenylate cyclase receptor-related signal transduction of human peripheral blood mononuclear cells. *Biochem Pharmacol* 44, 351–358 (1992).

81. Manning Jr, T. J. & Sontheimer, H. Bovine serum albumin and lysophosphatidic acid stimulate calcium mobilization and reversal of cAMP-induced stellation in rat spinal cord astrocytes. *Glia* 20, 163–172 (1997).

82. Knights, K. M., Mangoni, A. A. & Miners, J. O. Defining the COX inhibitor selectivity of NSAIDs: implications for understanding toxicity. *Expert Rev Clin Pharmacol* 3, 769–776 (2010).

83. Gam, J. *et al.* Ratiometric analyses at critical temperatures can magnify the signal intensity of FRET-based sugar sensors with periplasmic binding proteins. *Biosensors and Bioelectronics* 72, 37–43 (2015).

84. Ahmed, K., Zaidi, S. F., Rehman, R. & Kondo, T. Hyperthermia and protein homeostasis: Cytoprotection and cell death. *J Therm Biol* 91, 102615 (2020).

85. Li, Y. *et al.* The RAP1 guanine nucleotide exchange factor Epac2 couples cyclic AMP and Ras signals at the plasma membrane. *Journal of Biological Chemistry* 281, 2506–2514 (2006).

86. Gingras, A. R., Puzon-McLaughlin, W., Bobkov, A. A. & Ginsberg, M. H. Structural basis of dimeric Rasip1 RA domain recognition of the Ras subfamily of GTP-binding proteins. *Structure* 24, 2152–2162 (2016).

87. Chen, H., Farkas, E. R. & Webb, W. W. In vivo applications of fluorescence correlation spectroscopy. *Methods Cell Biol* 89, 3–35 (2008).

88. Zhang, Y. & Calderwood, S. K. Autophagy, protein aggregation and hyperthermia: a mini-review. *International Journal of Hyperthermia* 27, 409–414 (2011).

89. Mateju, D. *et al.* An aberrant phase transition of stress granules triggered by misfolded protein and prevented by chaperone function. *EMBO J* 36, 1669–1687 (2017).

90. Wolozin, B. Regulated protein aggregation: stress granules and neurodegeneration. *Mol Neurodegener* 7, 1–12 (2012).

91. Protter, D. S. W. & Parker, R. Principles and properties of stress granules. *Trends Cell Biol* 26, 668–679 (2016).

92. Greenwald, J. & Riek, R. Biology of amyloid: structure, function, and regulation. *Structure* 18, 1244–1260 (2010).

93. Schindelin, J. *et al.* Fiji: an open-source platform for biological-image analysis. *Nat Methods* 9, 676–682 (2012).

Nederlandse samenvatting voor leken

De opbouw van het menselijk lichaam is complex. Het bestaat uit biljoenen cellen die allemaal gespecialiseerd zijn in het uitvoeren van specifieke biologische processen. Denk hierbij bijvoorbeeld aan darmcellen, die gespecialiseerd zijn in het opnemen van voedingstoffen uit voedsel, of aan hartspiercellen, die gespecialiseerd zijn in het ritmisch samentrekken van het hart. Om te zorgen dat zulke processen op de juiste manier uitgevoerd worden is het van groot belang dat cellen met elkaar communiceren, en verstoringen in deze communicatie zijn vaak de aanleiding voor het ontstaan van ziektes en aandoeningen. Cellen kunnen onder andere met elkaar communiceren door het uitscheiden van specifieke signaalmoleculen, bijvoorbeeld een hormoon, dat herkent kan worden door andere cellen, die vervolgens op dit specifieke signaal kunnen reageren. Cellen kunnen zulke signaalmoleculen herkennen doormiddel van receptoreiwitten, die zich aan de buitenkant van het celoppervlak bevinden. Wanneer een receptoreiwit een specifiek signaalmolecuul herkent, verandert deze receptor van vorm. Door deze vormverandering wordt er binnenin de cel biochemische signaaltransductieroutes gestart, waardoor de cel uiteindelijk op het signaal kan reageren. Een enorm belangrijke signaaltransductieroute is de cyclisch adenosinemonofosfaat (afgekort: cAMP) signaaltransductieroute. In deze signaaltransductieroute wordt er binnenin de cel cAMP aangemaakt wanneer een zogeheten G-proteïnegekoppelde receptor (afgekort: GPCR) een specifiek signaal herkent. cAMP zal vervolgens binnenin de cel een grote hoeveelheid enzymen activeren of juist deactiveren, maar heeft uiteindelijk ook invloed op welke genen in deze cel tot uiting komen. cAMP wordt vervolgens afgebroken door fosfodiësterase enzymen. Deze signaaltransductieroute is betrokken bij een enorme hoeveelheid biologische processen in het menselijk lichaam, die het functioneren van vrijwel alle organen beïnvloeden.

Omdat de cAMP signaaltransductieroute zo belangrijk voor het menselijk lichaam is, is er veel onderzoek gedaan naar hoe deze signaaltransductieroute precies werkt, maar ook naar het ontwikkelen van nieuwe technieken om de cAMP signaaltransductieroute beter te kunnen onderzoeken. Hierin heeft de onderzoeksgroep waarin deze stage is uitgevoerd de afgelopen 20 jaar een grote bijdrage geleverd, met name door het ontwikkelen van een moleculaire biosensor die veranderingen in de cAMP concentratie binnenin een cel aangeeft. Deze cAMP biosensor is onder andere opgebouwd uit een eiwit dat fluorescent is. Oftewel, dit eiwit kan licht met een bepaalde golflengte absorberen, en zal vervolgens dit licht weer met een langere golflengte terug uitstralen. Hoeveel nanoseconden het duurt voordat het geabsorbeerde licht weer door de biosensor uitgestraald wordt is verschillend wanneer er wél of géén cAMP in de cel aanwezig is. Deze zogeheten 'fluorescentie levensduur' kunnen wij detecteren met een supergevoelige microscoop, waardoor de cAMP concentratie binnenin een cel onder de microscoop gemeten kan worden. Omdat de cAMP biosensor uit eiwit bestaat kan deze gemakkelijk in cellen ingebracht worden, namelijk door de DNA code die codeert voor het biosensor eiwit doormiddel van genetische modificatie in het DNA van de cel in te voegen. Deze cAMP biosensor is tijdens deze stage gebruikt om twee verschillende onderzoeksprojecten naar de cAMP signaaltransductieroute uit te voeren.

Zuurstof is essentieel voor het functioneren van het menselijk lichaam. Echter komen er in bepaalde weefsels binnen het menselijk lichaam wél zuurstofarme omstandigheden voor, ook wel hypoxie genoemd. Het belangrijkste voorbeeld hiervan zijn tumoren, die door ongecontroleerde groei vaak een slechte toevoer van zuurstofrijk bloed hebben. Tumorcellen moeten zich vervolgens aanpassen om te kunnen overleven en groeien in hypoxie, wat uiteindelijk leidt tot zeer agressieve tumoren die resistenter zijn tegen chemotherapie, en dus leidt tot een slechte prognose voor de patiënt. Omdat een aantal gepubliceerde wetenschappelijk onderzoeken hebben aangetoond dat de cAMP signaaltransductieroute een rol speelt in de aanpassing aan hypoxie, is de doelstelling van dit eerste project om te onderzoeken hoe hypoxie de werking van de cAMP signaaltransductieroute beïnvloed. Hierbij is specifiek gefocust op het effect van hypoxie op de activatie van de cAMP signaaltransductieroute door GPCRs, en op de afbraak van cAMP door fosfodiësterase enzymen. Tijdens dit onderzoek is gebruik gemaakt van de cAMP biosensor, een supergevoelige microscoop om de fluorescentie levensduur van de biosensor te detecteren, en een op maat gemaakte zuurstofdichte kamer waarin hypoxie gecreëerd konden worden, die perfect onder de microscoop past. In experimenten waarin cellen gestimuleerd werden met oplopende concentraties van signaalmoleculen die GPCRs

stimuleren om de cAMP signaaltransductieroute te activeren, zijn geen verschillen gevonden tussen de activatie van de cAMP signaaltransductieroute onder zuurstofrijke en zuurstofarme omstandigheden. Vervolgens zijn twee verschillende technieken gebruikt om een plotse cAMP uitbarsting in de cellen te veroorzaken, waarna vervolgens gemeten kon worden hoe snel cAMP in de cellen werd afgebroken door fosfodiësterase enzymen. Hierbij zijn ook geen verschillen gevonden tussen zuurstofrijke en zuurstofarme omstandigheden. Daarom is de conclusie van dit project dat zuurstofconcentratie geen directe invloed heeft op de activatie en afbraak van de cAMP signaaltransductie route.

Naast zuurstoftoevoer is ook het onderhouden van een optimale lichaamstemperatuur (37°C) essentieel voor het functioneren van het menselijk lichaam. Onze cellen bezitten daarom eiwitten die temperatuurgevoelig zijn, waardoor cellen temperatuursveranderingen kunnen meten, daarop kunnen reageren, en dit kunnen communiceren aan andere cellen. Denk bij zulke reacties bijvoorbeeld aan het vernauwen van bloedvaten in de kou om de lichaamstemperatuur optimaal te houden, of een pijngevoel bij contact met te warm water om te voorkomen dat je verbrand. Een aantal gepubliceerde wetenschappelijke onderzoeken suggereren dat de cAMP signaaltransductieroute mogelijk een rol speelt in het meten van en reageren op temperatuursveranderingen. Daarom is de doelstelling van dit tweede project om te onderzoeken óf en hoe de cAMP signaaltransductieroute beïnvloed wordt door temperatuursveranderingen. Tijdens dit onderzoek is wederom gebruik gemaakt van de cAMP biosensor, een supergevoelige microscoop om de fluorescentie levensduur van de biosensor te detecteren, en een incubator met temperatuurregulatie die perfect onder de microscoop past. Door deze incubator kunnen we cellen blootstellen aan snelle, nauwkeurige temperatuursveranderingen. In experimenten waarin cellen werden blootgesteld aan verhoogde temperaturen observeerden wij dat de fluorescentie levensduur van de cAMP biosensor langer werd, wat gelijk staat aan een verhoging in cAMP concentratie. Verschillende andere experimentele benaderingen werden uitgevoerd om te verifiëren dat de cAMP concentratie ook daadwerkelijk omhoog ging in cellen die zijn blootgesteld aan verhoogde temperaturen. Uit deze experimentele benaderingen bleek echter dat dit niet het geval was, wat betekent dat het fluorescentie levensduur-effect dat op hogere temperaturen geobserveerd werd een onbedoeld artefact is. Hierom concluderen wij dat deze biosensor niet gebruikt kan worden om op hogere temperaturen de cAMP signaaltransductieroute te onderzoeken. Wél werden nog enkele observering gedaan waaruit blijkt dat dit artefact waarschijnlijk niet door enkel verhoogde temperatuur veroorzaakt wordt, maar dat een cellulaire adaptatie om met verhoogde temperaturen om te gaan mogelijk actief een rol speelt in dit onbedoelde artefact, waarbij cAMP dus niet betrokken is.
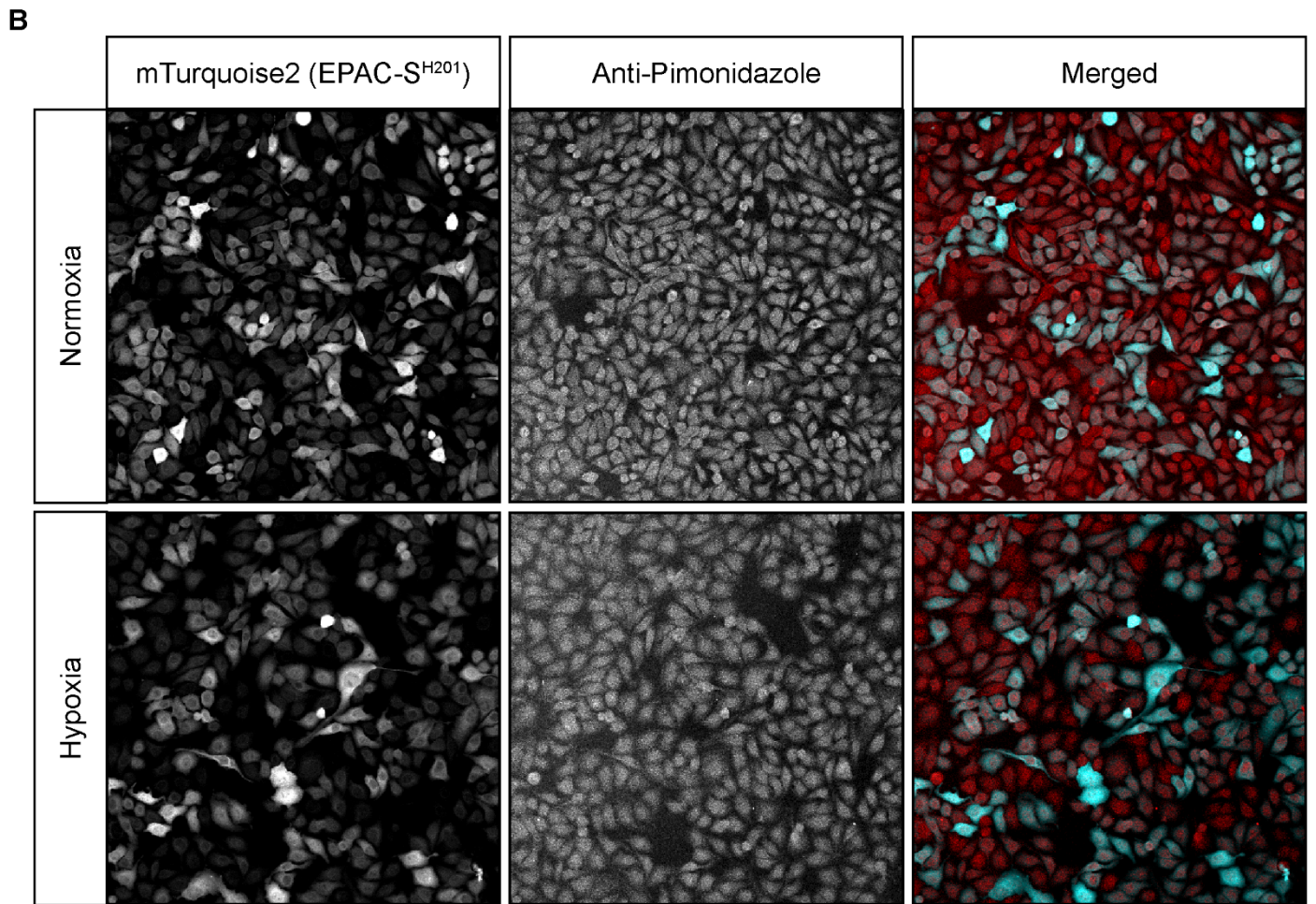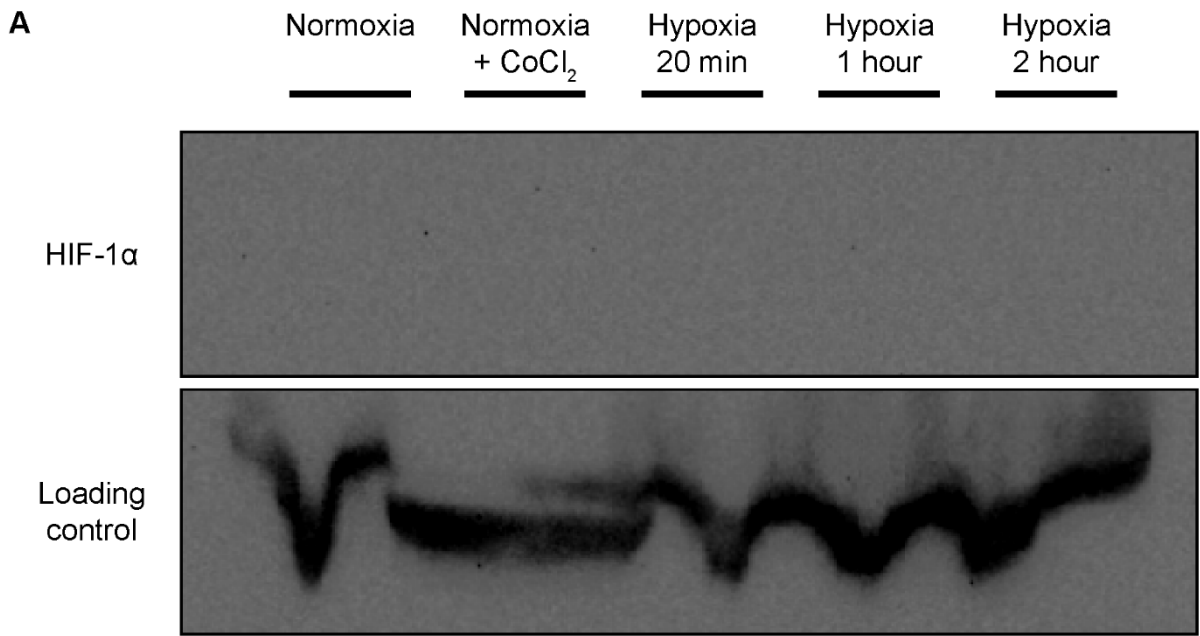
Supplementary Figures
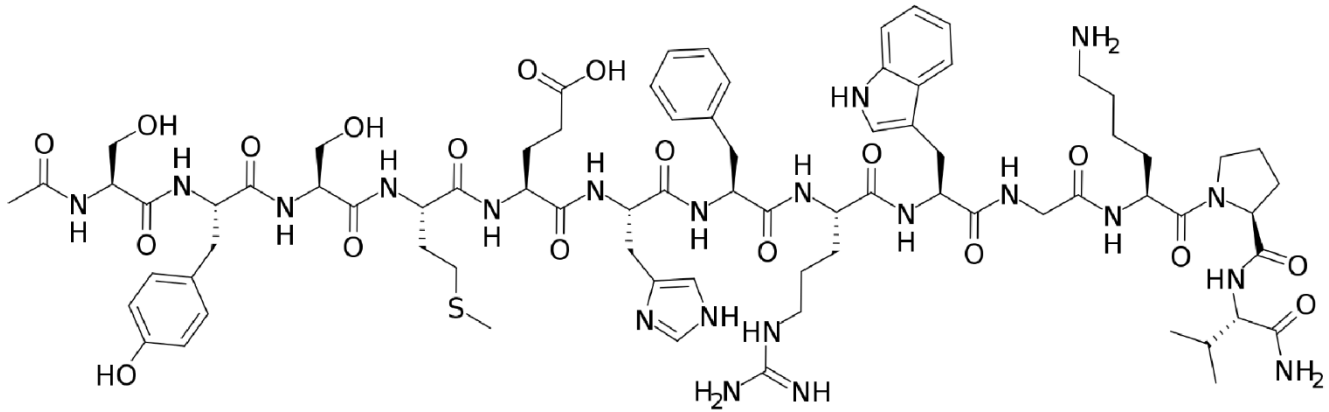

Supplementary Figure 1. The amphipathic structure of **α-melanocyte-stimulating** hormone.
Shown is the structural formula for α-melanocyte-stimulating hormone. Hydrophilic and hydrophobic amino acids are highlighted.

Supplementary Figure 2. Inconclusive hypoxia chamber validation experiments.
(A) Western Blots for HIF1α and alpha-tubulin (loading control) using lysate of HeLa EPAC-S^{H201} cells exposed to 20 minute normoxia (+ 6 hour 150 µM CoCl$_2$ pre-treatment as positive control) or various timeframes of hypoxia, as indicated. The positive control did not show the expected result (n=2). (B) Immunostainings for pimonidazole in HeLa EPAC-S^{H201} cells exposed to 1 hour normoxia or hypoxia in presence of 10 µM pimonidazole. The negative control normoxia condition did not show the expected result (n=2).
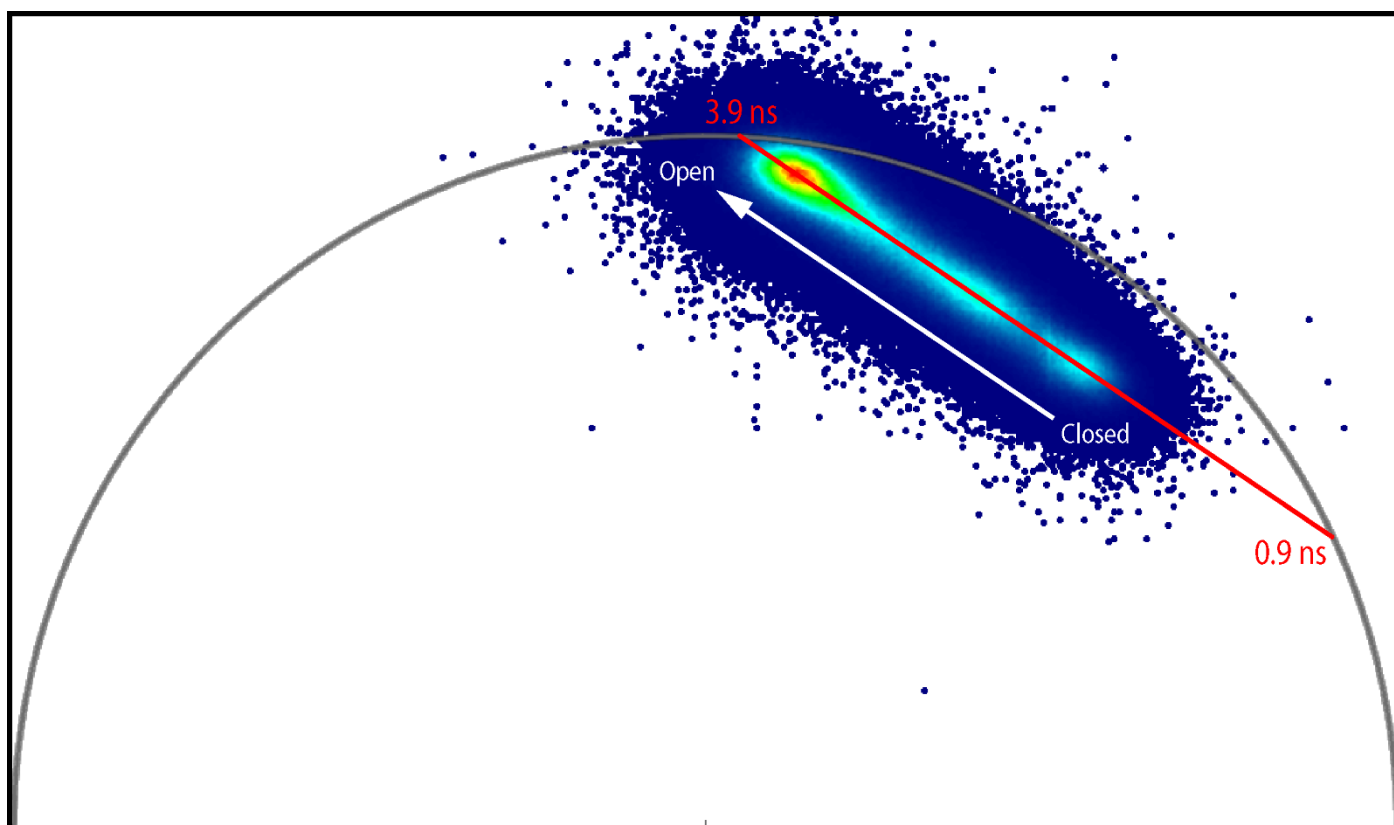
Supplementary Figure 3. Polar plot from which EPAC-S[H201] lifetime component values were derived.

Polar (phasor) plots are used to visualize fluorophore decay curves. Lifetime values are located on the semicircular axis, with lower lifetimes being located in the right-most part of the semicircular axis. Perfect mono-exponential decay curves will be localized on the semicircular line, while multi-exponential decay curves (like the EPAC-S[H201] FRET sensor decay curve) form a line within the semicircle. This is shown in this polar plot, based on experimental data obtained with the EPAC-S[H201] FRET sensor in the hypoxic condition shown in Figure 3B. As cAMP concentration during the experiment increases, the fraction of EPAC-S[H201] biosensors in the open, low FRET, high lifetime state increases, causing their phasors to travel towards the higher lifetimes on the semicircular axis, forming a line. EPAC-S[H201] lifetime components of 0.9 and 3.9 ns were obtained by extrapolating where the phasor line intercepts with the semicircular lifetime axis.